

**Supplemental Material for:**

**Garnet clinopyroxenite formation via amphibole-dehydration in continental arcs:  
evidence from Fe isotopes**

Emma S. Sosa<sup>1\*</sup>, Claire E. Bucholz<sup>1</sup>, Juan David Hernández-Montenegro<sup>1</sup>, Andrés Rodríguez-Vargas<sup>2</sup>,  
Michael A. Kipp<sup>3†</sup>, François L. H. Tissot<sup>3</sup>

<sup>1</sup> Division of Geological and Planetary Sciences, California Institute of Technology, Pasadena, CA  
91125

<sup>2</sup> Minerlab Limitada, Calle 51 Sur No 80i-34, 110861 Bogotá, DC., Colombia

<sup>3</sup> The Isotoparium, Division of Geological and Planetary Sciences, California Institute of Technology,  
Pasadena, CA 91125

† Now at Division of Earth and Climate Sciences, Duke University, Durham, North Carolina 27708

**\*Email:** [sosa45nh@gmail.com](mailto:sosa45nh@gmail.com)

## Supplemental Material

### Additional information on methods

Page 2-3 *Petrography, EMPA, and chemical purification of Fe*

### Supplemental figures

Page 4 *Fig. S1: Compositional RMSE P-T maps for  $\langle F \rangle_{\text{amph}}$  calculation*  
Pages 5-6 *Fig. S2: Compositional RMSE P-T maps for  $\langle F \rangle_{\text{cpx}}$  calculation*  
Page 7 *Fig. S3: Xenoliths classification on IUGS plag-px-hbl ternary*  
Page 8 *Fig. S4: Whole-rock trace element chemistry from Mercaderes xenoliths*  
Pages 9-10 *Fig. S5: Garnet, cpx, and amphibole trace element chemistry by sample*  
Page 11 *Fig. S6: Summary of trace element mineral chemistry*  
Page 12 *Fig. S7:  $\delta^{56}\text{Fe}$  vs.  $\delta^{76}\text{Fe}$  and  $\delta^{56}\text{Fe}$  measured vs. calculated*

### Inter-mineral Fe isotope fractionation

Page 13 *Comparison to previous studies*  
Page 14 *Fig. S8: Inter-mineral Fe isotope fractionation*

### Modeling

Page 15-18 *Additional modeling information*  
Page 19 *Fig. S9: Modal abundances of amphibole predicted by Perple\_X vs. MELTS*  
Page 19 *Fig. S10: Force constant estimates and Fe diffusion profiles*  
Page 20 *Fig. S11: Lava composition used in fractional crystallization modeling*  
Page 21 *Fig. S12: Additional modeling results*  
Page 22-23 *Fig. S13: Sensitivity tests of fractional crystallization models*  
Page 24 *Fig. S14: Isotopic evolution of cumulates and their parental melts*  
Page 25 *Fig. S15: Sensitivity tests for amphibole dehydration model*

### Mineral composition isopleths

Page 26-27 *Sample XC-MH-8*  
Page 28-29 *Sample XC-MP2-5*  
Page 30-31 *Sample XC-MH-6*

## **Additional information on methods**

### ***Petrography***

For each XRF session on the Bruker M4 Tornado  $\mu$ -EDXRF spectrometer, six to eight thin sections (mounted on either  $27 \times 46$  mm or 1" round glass slides) were loaded into the spectrometer and placed under a 20-mbar vacuum. Each thin section was mapped individually using a step size of 30  $\mu$ m and a 10 ms dwell time per measurement. X-ray conditions during analysis were a 50 kV voltage, 599  $\mu$ A beam current, and 30  $\mu$ m beam diameter. Depending on the dimensions and size of the mapped area, each thin section map took between 2 and 4 hours to acquire. For the principal component analysis (PCA) calculations used to determine mineral modes, the software groups individual measurements into phases based on similarities in the relative intensity of measured elements. For the Mercaderes samples, we found the software was best able to distinguish between the phases observed through optical petrography (i.e., garnet, clinopyroxene, orthopyroxene, amphibole, scapolite, plagioclase, and titanite) when we performed the PCA with Al, K, Ca, Mn, Fe, Cr, Na, Ti, and Mg.

### ***Mineral chemistry (major and trace element)***

For major element electron microprobe analyses, a 15 kV acceleration voltage, 25 nA beam current, and a 1-10  $\mu$ m spot size (1.0  $\mu$ m for garnet, pyroxene, and plagioclase, 10  $\mu$ m for amphibole) were used. Peak and background count times for all measured elements and a list of EPMA standards are given in Supplemental Table S3. In general, 15 to 50 core analyses and 5 to 20 rim analyses were collected for each major phase in every sample. The electron microprobe data was reduced using a modified ZAF procedure (CITZAF, Armstrong, 1995). The detection limits for these conditions were: <0.01 wt.% for Si, Al, Mg, Ca, K, and Cl, <0.02 wt.% for Ti, Fe, Na, Cr, Mn, and <0.03 wt.% for F. For trace element LA-ICP-MS analyses, sample surfaces were pre-ablated for 10 seconds for each analysis. Data were collected for 30 seconds, totaling 40 seconds of ablation, followed by 40 seconds of washout. Each laser shot was performed at a 10 Hz repetition rate, and we used a He carrier gas. An 80  $\mu$ m spot size was used for both analytical sessions. Typically, 3-10 core analyses and 2-6 rim analyses were generally obtained for each phase in each sample. Every fifteen to twenty unknown sample measurements were bracketed with analysis of standards NIST 610 and BCR-2, which were used to construct calibration curves.

### ***Chemical purification of Fe and presentation of data***

All samples were digested in a mixture of concentrated HF and HNO<sub>3</sub> in a 2:1 ratio at 100 °C for 5 hours. These samples were fully dried and redigested in concentrated HCl and HNO<sub>3</sub> in a 3:1 ratio at 140 °C for 12 hours before being fully dried again. For the final digestion step, samples were fluxed in concentrated HCl and HNO<sub>3</sub> at 140 °C for 12 hours, but in a 2:1 ratio. Samples were then completely dried and fluxed in concentrated HCl at 180 °C for two days before being brought into a 6 M HCl solution before column chemistry. Samples were loaded into 10 mL polyethylene chromatography columns filled with 1 mL of BioRad AG1-X8 200-400 mesh anion exchange resin. Matrix elements were flushed from the columns with 8 mL of 0.4 M HCl before 8 mL of 0.4 M HCl was passed through the column to recapture the purified Fe. We performed column chemistry twice to ensure all matrix elements were removed from the purified sample. To ensure a complete matrix match between the samples and our IRMM-524b standard solution, samples were fully dried and fluxed for 12 hours in concentrated HNO<sub>3</sub> at 140 °C before being dried and taken up in 5 mL of 0.3 M HNO<sub>3</sub> run acid. Samples were fluxed in run acid at 130 °C for 12 hours prior to the start of the analytical session.

Because more measurements are made of the IRMM-524b standard than any sample during standard bracketing, the standard deviation of IRMM-524b better represents the true uncertainty of the session (Dauphas et al., 2009), and we thus opted to report errors based on the standard deviation of the IRMM-524b standard rather than the samples [error =  $2 \cdot \text{SD}_{\text{IRMM-524b}} / (n_{\text{sample}})^{0.5}$ ]. Errors were also recalculated using the standard deviation of each sample [error =  $2 \cdot \text{SD}_{\text{sample}} / (n_{\text{sample}})^{0.5}$ ] and are given in the Supplemental Data (Table S15). For  $\delta^{56}\text{Fe}$ , the errors calculated using the two methods are consistently within 0.025‰ of each other, with errors calculated from the 2SD of the standard generally 0.005‰ higher than those calculated using sample 2SD.

## Temperature, pressure, and density estimates for Mercaderes xenoliths

For samples containing garnet and clinopyroxene, pressure and temperature were estimated by simultaneously solving the geothermometer of Ravna (2000) and geobarometer of Beyer et al. (2015). For samples with core-to-rim zoning, these calculations were performed separately with electron microprobe data taken from the core, mantle, and rim of both phases. Within each zone (i.e., all core, mantle, or rim points), the geothermometer and geobarometer were solved multiple times, varying and garnet and clinopyroxene composition (particularly, Mn, Ca, Fe, and Mg in garnet and Fe, Mg, and Al in clinopyroxene). The range in P-T determined for grain cores, mantle, and rims for each sample represents the compositional variation observed in each zone. We used a similar method to evaluate the uncertainty in our pressure-temperature calculations for amphibole-plagioclase thermometry (Holland and Blundy, 1994) and barometry (Anderson and Smith, 1995), where the geothermometer and geobarometer were solved simultaneously while varying amphibole and plagioclase compositions.

For the samples where the observed  $\Delta^{56}\text{Fe}_{\text{cpx-gar}}$  and  $\Delta^{56}\text{Fe}_{\text{amph-gar}}$  were used to estimate appropriate force constants for clinopyroxene and amphibole, we also constrained temperature by constructing pseudosections with *Perple\_X* for each sample using whole-rock compositions. From these pseudosections, the stability fields of garnet, clinopyroxene, and (when present) amphibole were extracted, along with the endmember components of jadeite, calcium tschermakite, diopside, pyrope, grossular, and almandine. Isopleths of these endmember components were then compared to measured mineral chemistry for each sample and used to generate maps in pressure-temperature space of the root-mean-square error (RMSE). The results of these calculations are shown in Supplemental Figures S1 and S2, with the red areas indicating a high RMSE and the blue regions a low RMSE (i.e., a better fit for the measured data). Combining these models with the mineral equilibria geothermobarometry, we determined appropriate temperature estimates to use for each sample in calculating clinopyroxene and amphibole force constants. Examples of the mineral composition isopleths used to construct these RMSE maps are given at the end of the supplement.

Using these pressure-temperature estimates and whole-rock compositions (either measured whole-rock values or estimated values calculated using mineral chemistry and modes), we used the *meemum* function in *Perple\_X* to estimate mineral densities at the equilibrium pressure and temperature for each sample. These modeling results were then used to estimate bulk densities for the xenoliths at depth (Supplemental Data, Table S9). Densities at the preferred pressure and temperature conditions for each sample were also calculated using the approach of Abers and Hacker (2016). These values are also given in the Supplemental Data (Table S9) for comparison and are consistently within 0.1 g/cm<sup>3</sup> of the densities obtained through *Perple\_X* modeling.

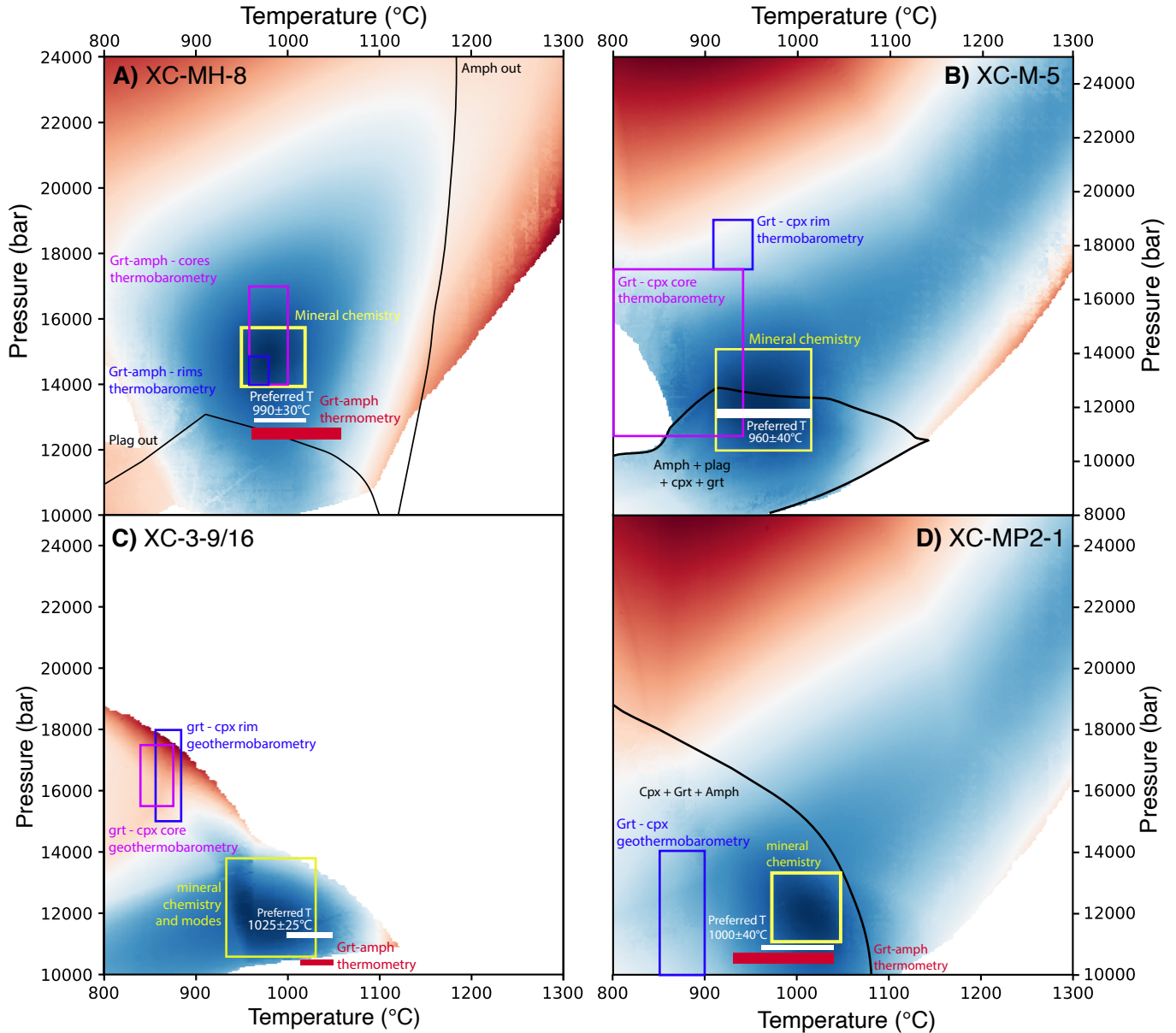


**Figure S1:** Map of RMSE in pressure-temperature space for garnet and clinopyroxene compositions and mineral modes for samples used to calculate  $\langle F \rangle_{\text{amph}}$  from  $\Delta^{56}\text{Fe}_{\text{amph-gar}}$ . Colored boxes denote the equilibrium pressure-temperature range for the sample as indicated by mineral equilibria thermobarometry and white bars indicate the temperature range used to calculate the amphibole force for each sample. **A)** XC-MH-8: using a temperature of  $990 \pm 30$  °C we calculate  $\langle F \rangle_{\text{amph}} = 237 \pm 6$  N/m for this sample. **B)** XC-M-5: for this sample we use a temperature estimate of  $960 \pm 40$  °C and calculate  $\langle F \rangle_{\text{amph}} = 257 \pm 5$  N/m. **C)** XC-3-9/16: using a temperature estimate of  $1025 \pm 25$  °C we calculated  $\langle F \rangle_{\text{amph}} = 249 \pm 5$  N/m for this sample. **D)** XC-MP2-1: for this sample we used a temperature of  $1000 \pm 40$  °C and calculated  $\langle F \rangle_{\text{amph}} = 200 \pm 6$  N/m. All errors come from the uncertainties in temperature estimates. The weighted average of these values,  $\langle F \rangle_{\text{amph}} = 232 \pm 21$ , is used in modeling.

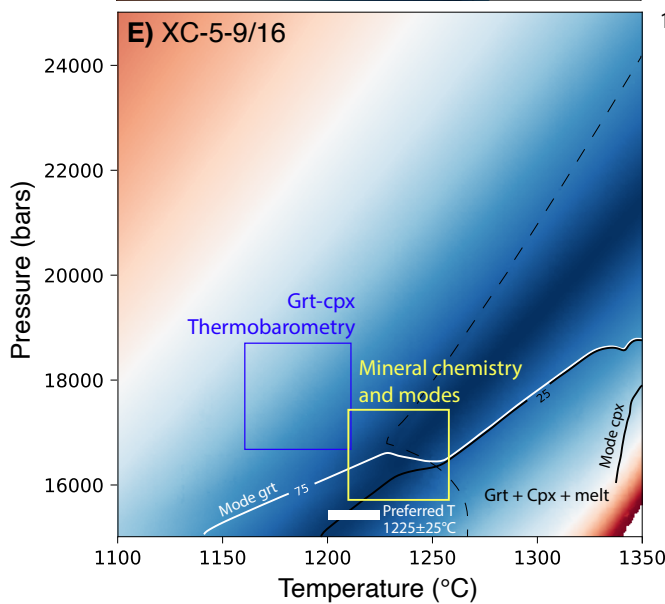
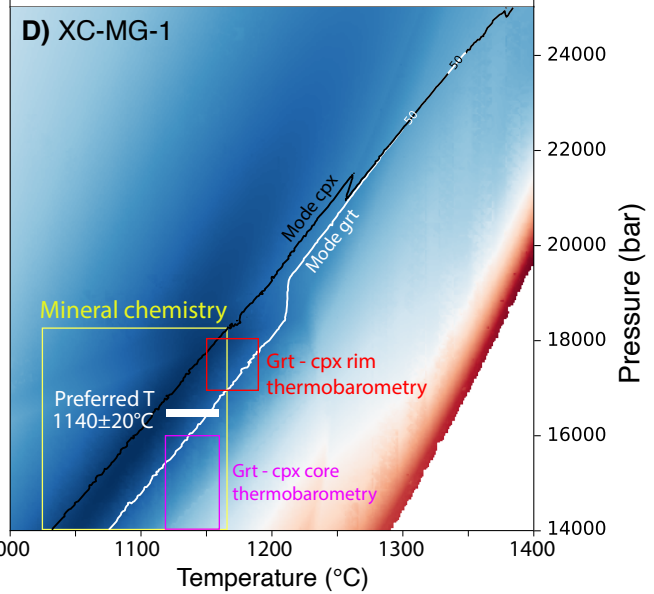
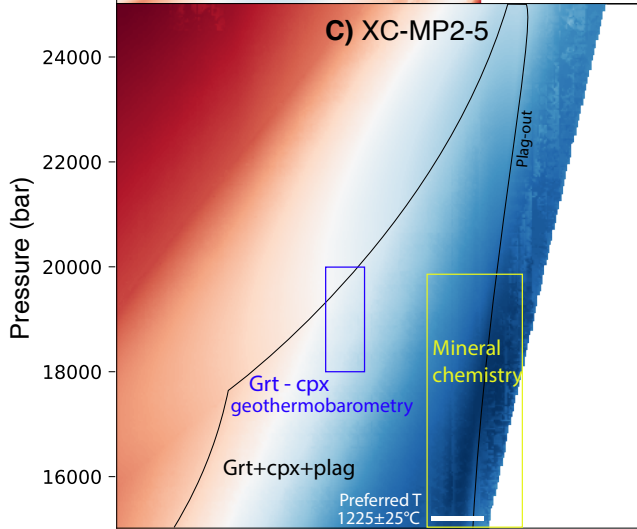
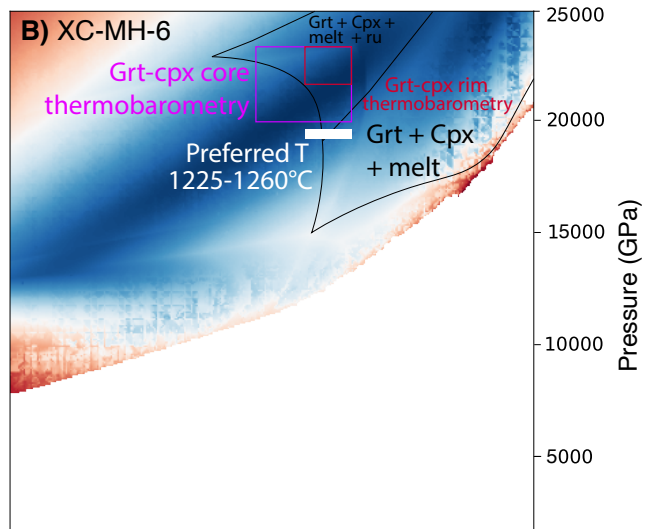
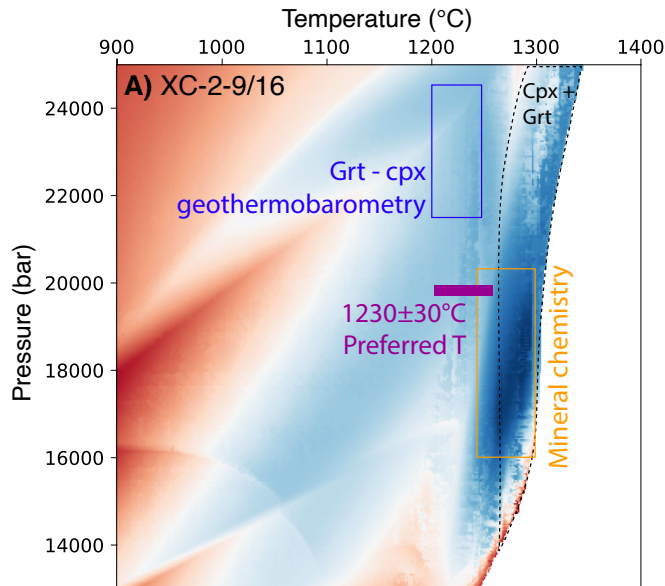


**Figure S2 (previous page):** Map of RMSE in pressure-temperature space for garnet and clinopyroxene compositions and mineral modes for samples used to calculate  $\langle F \rangle_{\text{cpx}}$  from  $\Delta^{56}\text{Fe}_{\text{cpx-gar}}$ . **A)** XC-2-9/16: using a temperature of  $1230 \pm 30$  °C we calculated  $\langle F \rangle_{\text{cpx}} = 243 \pm 4$  N/m for this sample. **B)** XC-MH-6: while the RMSE map does not allow us to further constrain temperature for this sample, the P-T conditions given by thermobarometry are consistent with the results of Perple\_X modeling, and using a temperature range of  $1225 - 1226$  °C, we calculate  $\langle F \rangle_{\text{cpx}} = 235 \pm 5$  N/m for this sample. **C)** XC-MP2-5: for this sample, garnet-clinopyroxene thermobarometry indicated lower temperatures than are indicated by our Perple\_X modeling, likely due to uncertainties in cpx  $\text{Fe}^{+2}$ . Instead, we use a temperature estimate of  $1225$  °C and estimate a  $\langle F \rangle_{\text{cpx}}$  of  $228 \pm 6$  N/m. **D)** XC-MG-1: for this sample, we use a temperature estimate of  $1140 \pm 20$  °C and calculate  $\langle F \rangle_{\text{cpx}} = 243 \pm 4$  N/m. **E)** XC-5-9/16: using an estimated temperature of  $1225 \pm 25$  °C, we calculate  $\langle F \rangle_{\text{cpx}} = 235 \pm 4$  N/m for this sample. The weighted average of these results yields a clinopyroxene force constant of  $227 \pm 17$  N/m.

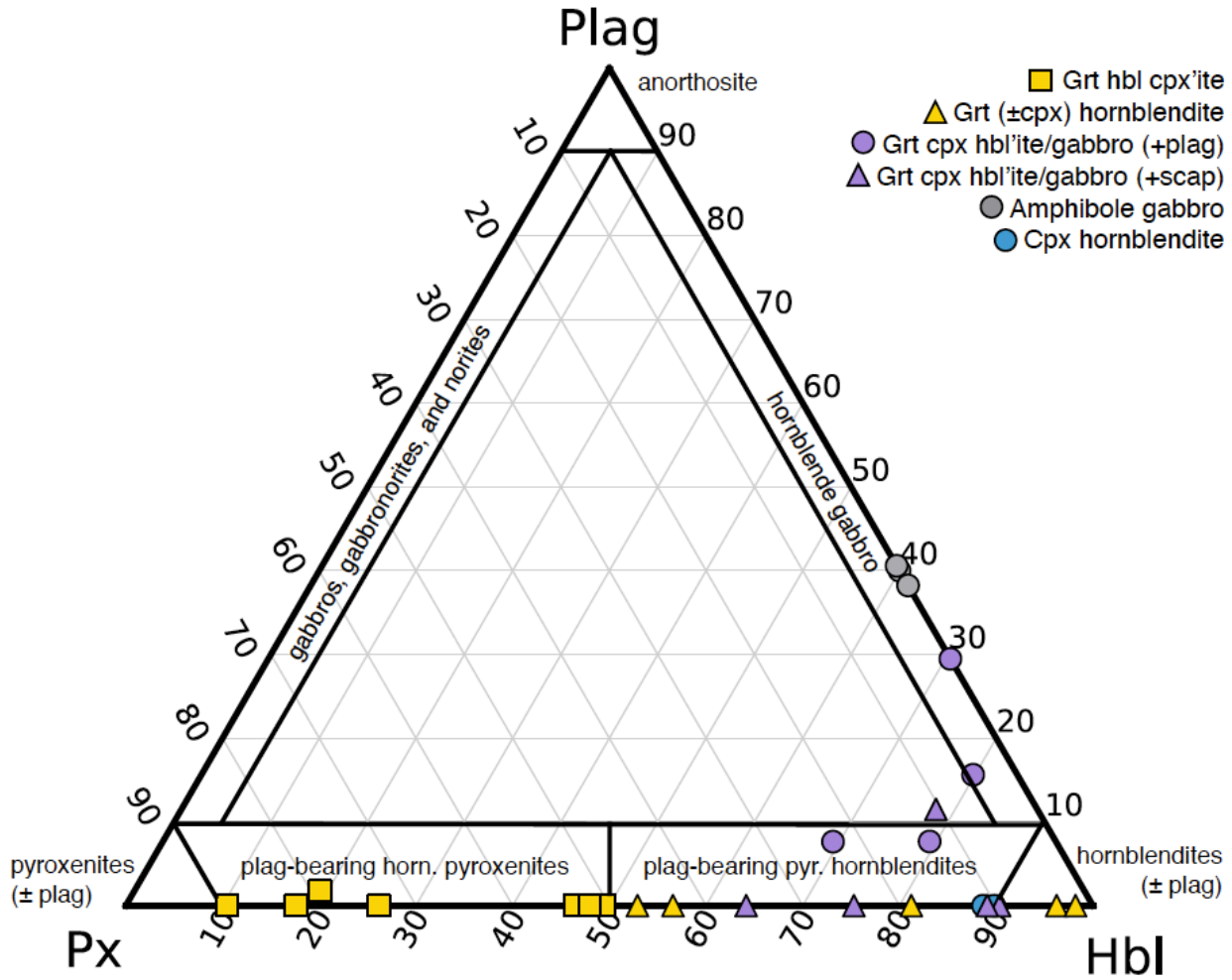


**Figure S3:** Classification of Mercaderes xenoliths on IUGS plagioclase (plag), pyroxene (px), and hornblende (hbl) ternary. Rocks containing only garnet and clinopyroxene are not shown but would plot on the apex of the pyroxene region of the ternary.

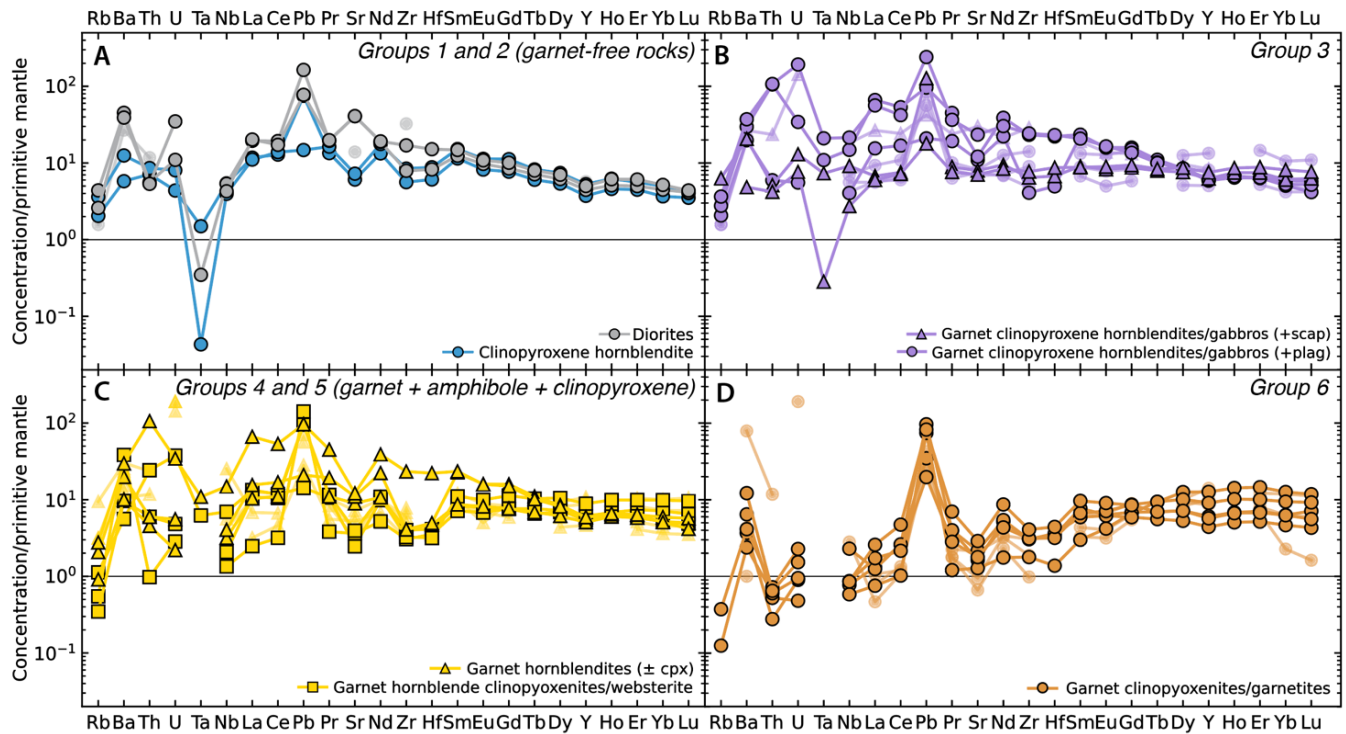


**Figure S4:** Whole-rock trace element chemistry from Mercaderes xenoliths. **A)** Diorites and clinopyroxene hornblende. **B)** Plagioclase or scapolite-bearing garnet clinopyroxene hornblende and gabbros. **C)** Garnet hornblende ( $\pm$  cpx) and garnet hornblende clinopyroxenite. **D)** Garnet clinopyroxenite. Data from Weber (1998) are represented by transparent symbols without borders.

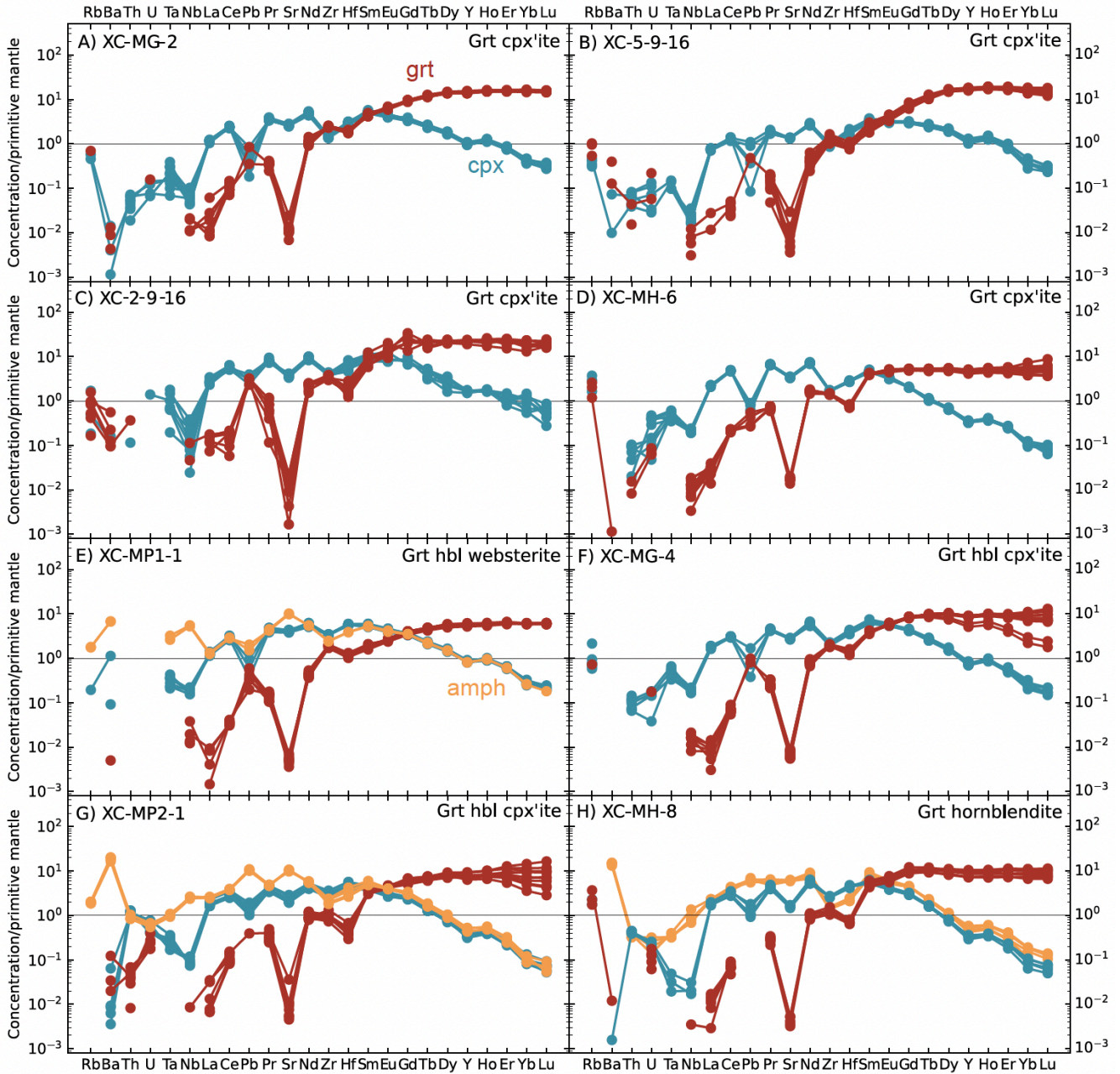


**Figure S5a:** Core and rim trace element garnet (red), clinopyroxene (blue), and amphibole (orange) mineral chemistry for Mercaderes xenoliths. **A)** Garnet clinopyroxenite XC-MG-2. **B)** Garnet clinopyroxenite XC-5-9-16. **C)** Garnet clinopyroxenite XC-2-9-1. **D)** Garnet clinopyroxenite XC-MH-6. **E)** Garnet hornblende websterite XC-MP1-1. **F)** Garnet hornblende clinopyroxenite XC-MG-4. **G)** Garnet hornblende clinopyroxenite XC-MP2-1. **H)** Garnet hornblende XC-MH-8. Unless noted, there is no systematic difference between core and rim compositions.

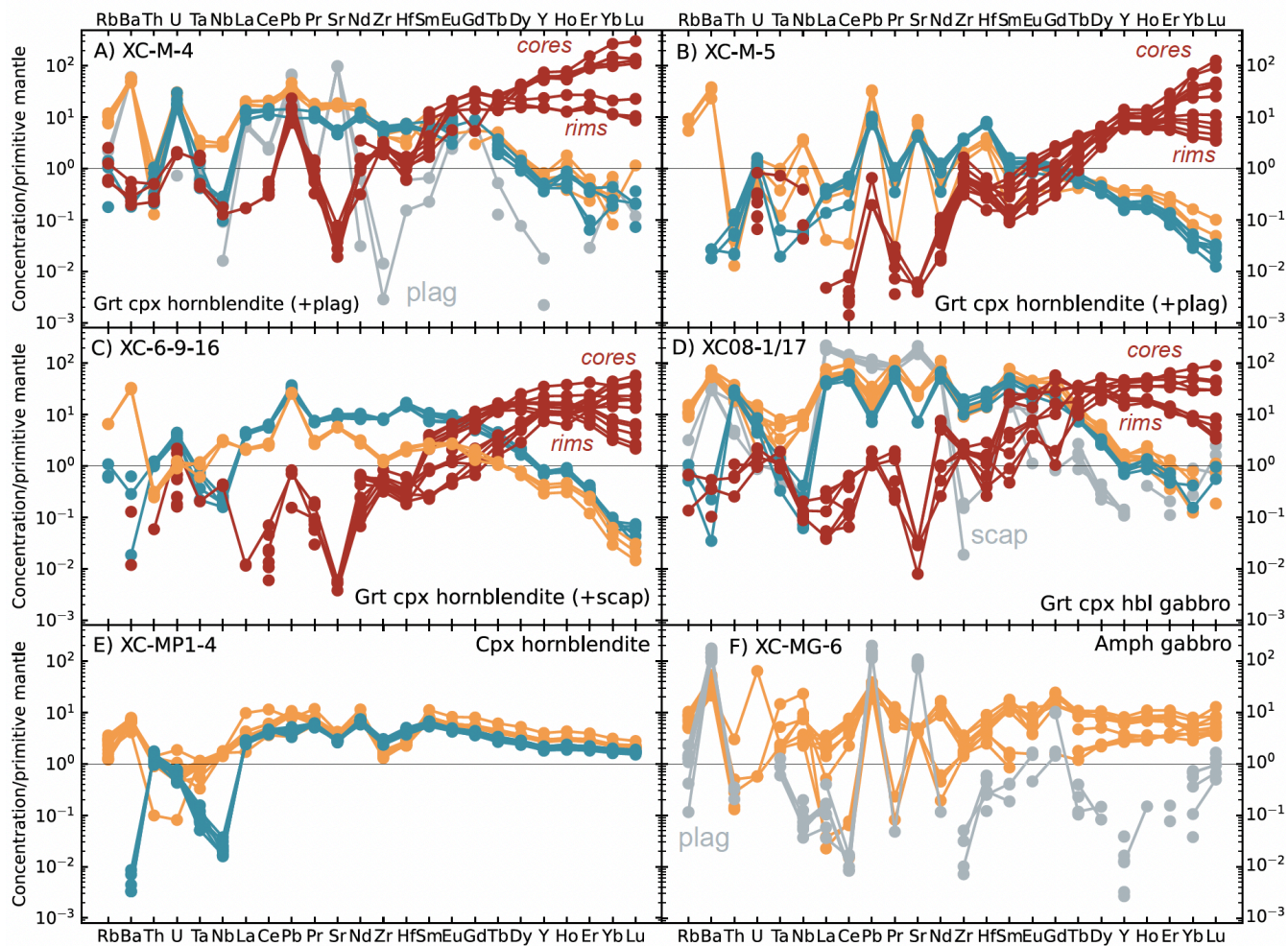


**Figure S5b:** Core and rim trace element garnet (red), clinopyroxene (blue), amphibole (orange), plagioclase (grey, labeled), and scapolite (grey, labeled) mineral chemistry for Mercaderes xenoliths. **A)** Plagioclase-bearing garnet clinopyroxene hornblendite XC-M-4. **B)** Plagioclase-bearing garnet clinopyroxene hornblendite XC-M-5. **C)** Scapolite-bearing garnet clinopyroxene hornblendite XC-M-4. **D)** Garnet clinopyroxene hornblende gabbro XC08-1/17. **E)** Clinopyroxene hornblendite XC-MP1-4. **F)** Diorite XC-MG-6. Unless noted, there is no systematic difference between core and rim compositions.

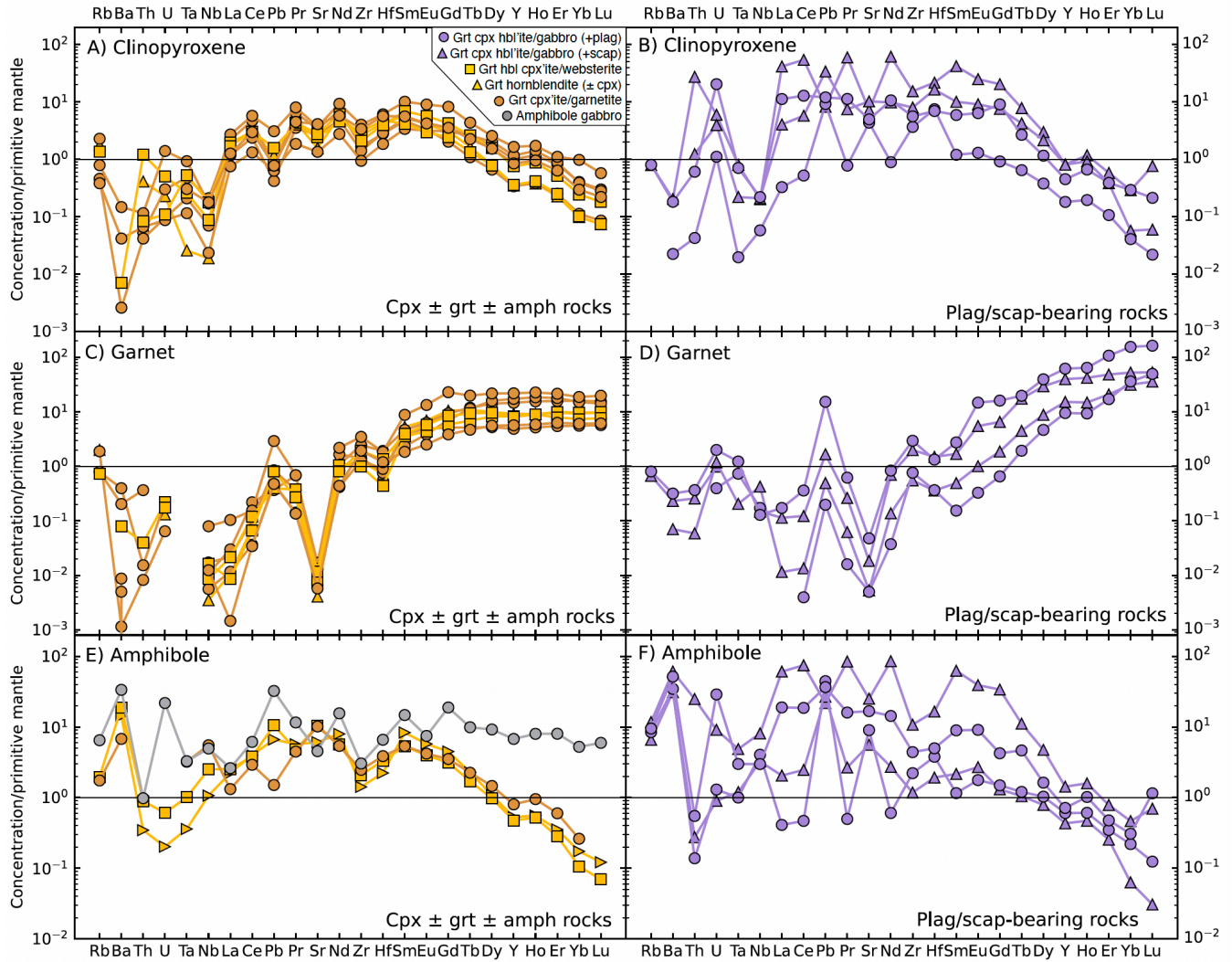


**Figure S6:** Summary of trace element average core mineral chemistry. Primitive mantle normalized spider diagrams for Mercaderes clinopyroxene (**A** & **B**), garnet (**C** & **D**), and amphibole (**E** & **F**) cores. Data for minerals from the plagioclase/scapolite-bearing garnet clinopyroxene hornblendites and gabbros (Group 2) are shown separately (panels **B**, **C**, and **D**) to emphasize the disequilibrium trace element patterns of these samples.

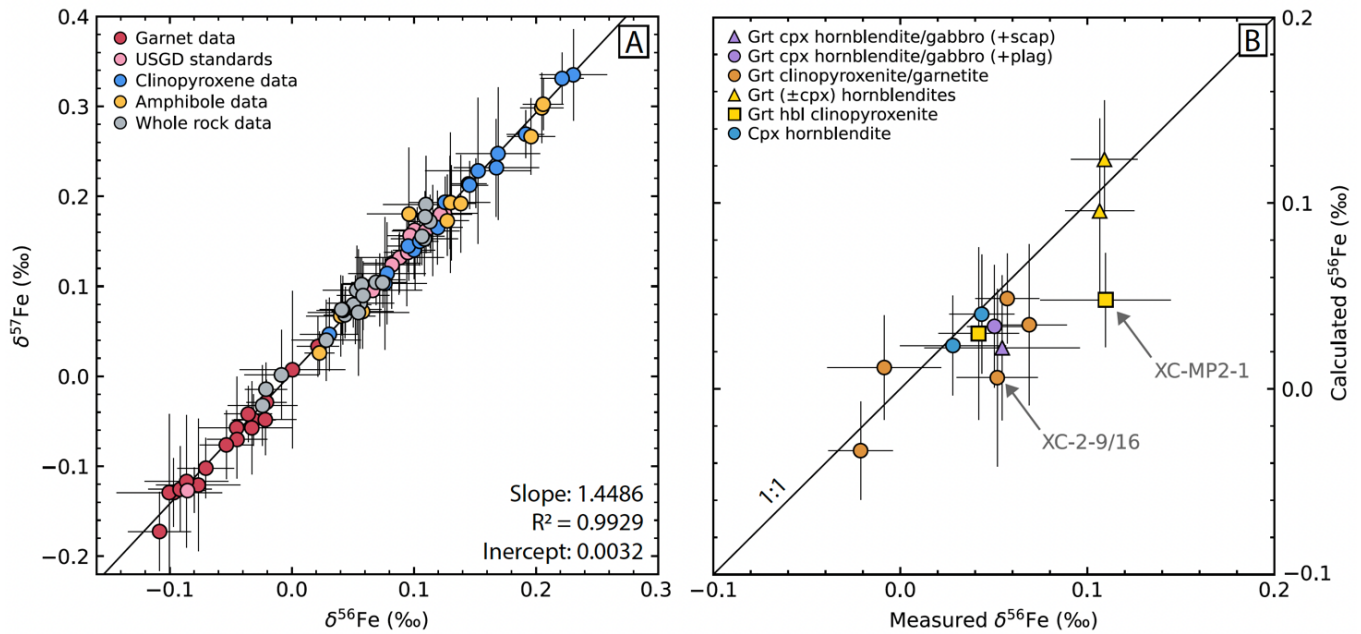


**Figure S7:** Quality assessment of Fe isotope data. **A)**  $\delta^{56}\text{Fe}$  vs.  $\delta^{57}\text{Fe}$  (‰) of all measured samples. A linear regression through the data gives a slope of 1.4486 and an intercept of 0.0032, in excellent agreement with the expected mass-dependent fractionation ( $\delta^{57}\text{Fe} \approx 1.5 \times \delta^{56}\text{Fe}$ , Dauphas et al., 2017) and illustrating the accuracy of our Fe isotope measurements. **B)** Measured vs calculated whole-rock Fe isotope composition of Mercaderes samples. Whole-rock compositions were calculated using the modes, densities, major element chemistry, and measured  $\delta^{57}\text{Fe}$  of minerals for each sample. Apart from samples XC-2-9/16 and XC-MP2-1, the measured and calculated values are within error of each other ( $\sim 0.03\%$ ).

### Inter-mineral Fe isotope fractionation

Clinopyroxene-garnet Fe isotope fractionation similar to that observed in the Mercaderes xenoliths ( $\Delta^{56}\text{Fe}_{\text{cpx-gar}} = +0.07$  to  $+0.33\text{‰}$ ) are also seen in eclogites from the Swiss Alps ( $\Delta^{56}\text{Fe}_{\text{cpx-gar}} = 0.29 \pm 0.14$ ; Beard and Johnson, 2004); Bohemian Massif ( $\Delta^{56}\text{Fe}_{\text{cpx-gar}} = +0.27$  to  $+0.42\text{‰}$ ; Beard and Johnson, 2004); the Dabie orogen belt, China ( $\Delta^{56}\text{Fe}_{\text{cpx-gar}} = +0.13$  to  $+0.48\text{‰}$ ; Li et al., 2016); the North Qaidam metamorphic belt, China ( $\Delta^{56}\text{Fe}_{\text{cpx-gar}} = +0.1$  to  $+0.37\text{‰}$ , ave. =  $+0.27\text{‰}$ ; Liang et al., 2022); eclogite xenoliths from kimberlite pipes ( $\Delta^{56}\text{Fe}_{\text{cpx-gar}} = 0.0$  to  $+0.34\text{‰}$ , ave. =  $+0.18\text{‰}$ ; Williams et al 2009); and garnet peridotites from the Czech Republic ( $\Delta^{56}\text{Fe}_{\text{cpx-gar}} = 0.24$  to  $+0.31\text{‰}$ ; Beard and Johnson, 2004) (Fig. S8a). Mantle-derived garnet websterite from the Cameroon Line ( $\Delta^{56}\text{Fe}_{\text{cpx-gar}} = +0.03$  to  $+0.08\text{‰}$ ; Williams et al., 2005) and metasomatized garnet peridotite from the Kaapvaal Craton ( $\Delta^{56}\text{Fe}_{\text{cpx-gar}} = +0.01$  to  $+0.11\text{‰}$ ; An et al., 2017) show less clinopyroxene-garnet fractionation than is observed in the Mercaderes samples.

Although Fe isotope data of coexisting amphibole and clinopyroxene are scarce in the literature, low degrees of inter-mineral fractionation similar to those observed in the Mercaderes samples ( $\Delta^{56}\text{Fe}_{\text{amph-gar}} = +0.23$  to  $+0.30\text{‰}$ ) have been reported in augite syenite from the Ilímaussaq Complex ( $\Delta^{56}\text{Fe}_{\text{cpx-amph}} = -0.03 \pm 0.05\text{‰}$ ; Schoenberg et al., 2009), a garnet pargasite websterite from the Cameroon Line ( $\Delta^{56}\text{Fe}_{\text{cpx-amph}} = -0.04 \pm 0.08\text{‰}$ ; Williams et al., 2005), cumulate xenoliths from Adak Island ( $\Delta^{56}\text{Fe}_{\text{cpx-amph}} = -0.01$  to  $+0.01\text{‰}$ ; Sosa et al., 2023), and metasomatized spinel lherzolite from the North China Craton ( $\Delta^{56}\text{Fe}_{\text{cpx-amph}} = -0.03$  to  $+0.01\text{‰}$ ; Zhao et al., 2015) (Fig. S8b). Greater clinopyroxene-amphibole isotopic fractionation is observed in retrograde eclogites from the Dabie orogen belt, China ( $\Delta^{56}\text{Fe}_{\text{cpx-amph}} = +0.13 \pm 0.10\text{‰}$ ; Li et al., 2016).

Inter-mineral isotopic fractionation between coexisting amphibole and garnet ranges from  $\Delta^{56}\text{Fe}_{\text{amph-gar}} = +0.10$  to  $+0.30\text{‰}$  and is consistently higher in the hornblendite ( $\pm$  scapolite/plagioclase) xenoliths ( $\Delta^{56}\text{Fe}_{\text{amph-gar}} = +0.23$  to  $+0.30\text{‰}$ ) than the clinopyroxenite specimens ( $\Delta^{56}\text{Fe}_{\text{amph-gar}} = +0.10$  to  $+0.17\text{‰}$ ) (Fig. S8c) While Fe isotope data for coexisting amphibole and garnet are also scarce in the literature, previous studies have reported levels of amphibole-garnet fractionation similar to our Mercaderes samples ( $\Delta^{56}\text{Fe}_{\text{amph-gar}} = +0.23$  to  $+0.30\text{‰}$ ) in banded iron formations ( $\Delta^{56}\text{Fe}_{\text{amph-gar}} = +0.29$  to  $+0.43\text{‰}$ ; Ye et al., 2020), retrograde eclogite ( $\Delta^{56}\text{Fe}_{\text{amph-gar}} = +0.09$  to  $+0.25\text{‰}$ ; Li et al., 2016), and one garnet pargasite websterite ( $\Delta^{56}\text{Fe}_{\text{amph-gar}} = +0.12 \pm 0.11\text{‰}$ ; Williams et al., 2005).

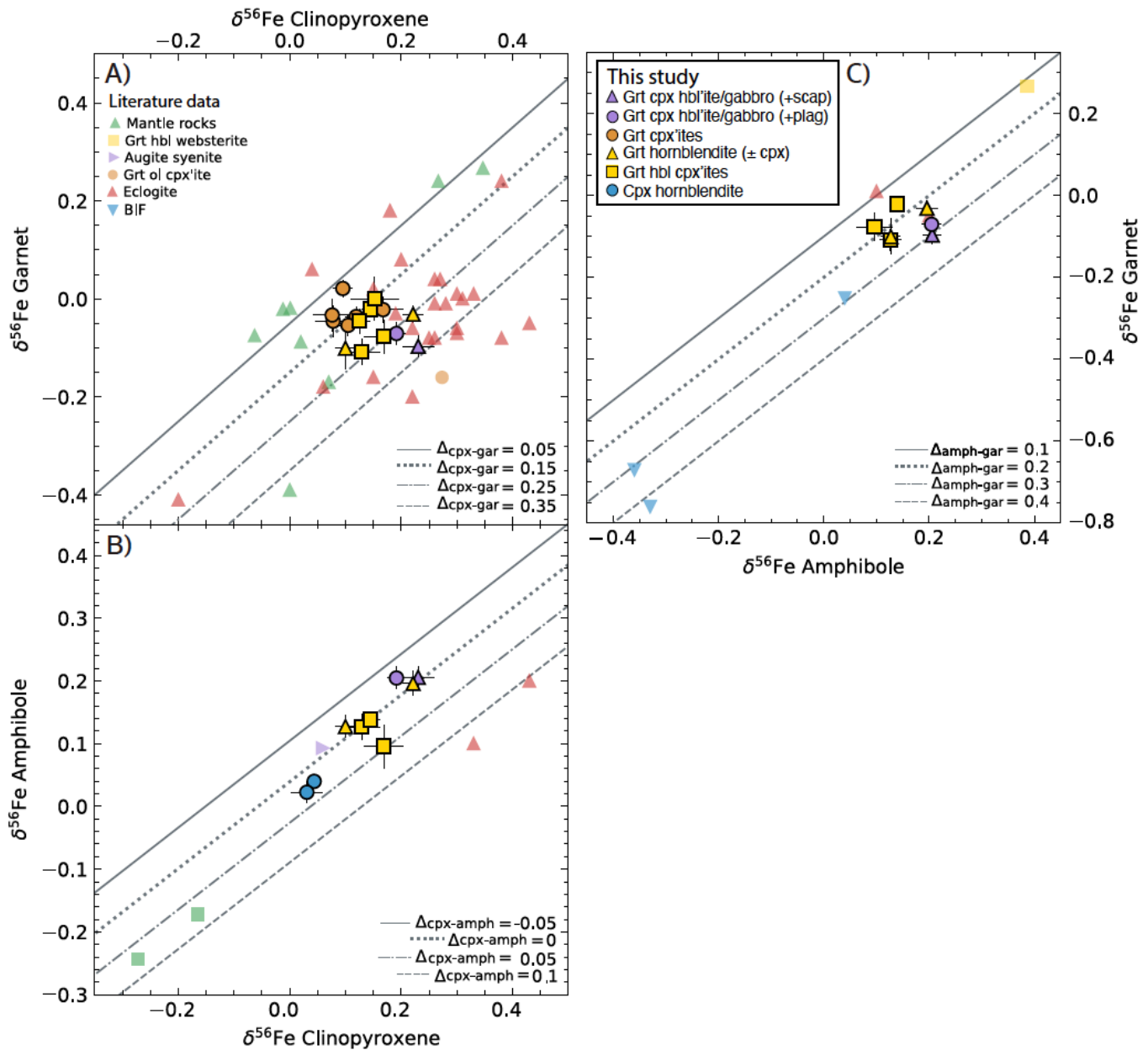


**Figure S8:** Inter-mineral Fe isotope fractionation for garnet, amphibole, and clinopyroxene mineral separates from Mercaderes compared to literature data. Eclogite data is from Beard and Johnson (2004), Williams et al. (2009), Li et al. (2016), and Liang et al. (2022). Mantle garnet peridotite, websterite, and clinopyroxenite data are from Williams et al. (2005), Beard and Johnson (2004), and An et al. (2017). Banded iron formation (BIF) data is from Ye et al. (2020). Syenite data is from Schoenberg et al. (2009).

## Additional modeling information and results

**Force constants:** As discussed in the text, amphibole and clinopyroxene force constants were estimated from their observed Fe isotope fractionation with coexisting garnet using the equation:

$$\Delta^{56}\text{Fe}_{\text{B-A}} = \delta^{56}\text{Fe}_{\text{B}} - \delta^{56}\text{Fe}_{\text{A}} = 2853[\langle F \rangle_{\text{B}} - \langle F \rangle_{\text{A}}]/T^2$$

While we ascribe all Fe in garnet to the almandine endmember, the samples likely also contain a small amount of andradite. This is supported by our garnet core  $\text{Fe}^{+3}/\Sigma\text{Fe}$  estimates, which range from 0.04 to 0.16 with an average value of 0.10. However, to our knowledge, the force constant of andradite has never been interrogated through an NRIXS-based study or first-principles calculations. While atomic theory suggests that  $\text{Fe}^{+3}$ -bearing andradite should have a higher force constant than  $\text{Fe}^{+2}$ -rich almandine, we do not have the data required to make a quantitative estimate. Future studies are required to resolve this issue, which is beyond the scope of the work presented here. We, therefore, elect to ascribe all Fe in garnet, both for the samples and our models, to the almandine endmember. Fe-oxides such as magnetite are not present in the solid model assemblages and are only observed in some xenoliths in trace abundances; thus, they were ignored for modeling purposes.

The amphibole and clinopyroxene force constants calculated for each sample are shown as a function of their equilibrium temperature estimate in Supplemental Figure S10a. If our temperature estimates were not associated with Fe isotope equilibrium, and Fe diffusion continued to lower temperatures, we would expect to see strong correlations between our calculated force constant estimates and temperature. The lack of any such correlations suggests that the temperatures used in calculations are appropriate estimates. This is not surprising, given the relatively slow diffusivity of Fe in garnet and clinopyroxene (Fig. S10b). Using the pre-exponential factor ( $D_0$ ) and activation energy ( $E$ ) of Fe in garnet and clinopyroxene, we can use the Arrhenius equation to estimate the Fe diffusion coefficient as a function of temperature:

$$D(T) = D_0 e^{(-E/RT)}$$

where  $T$  is temperature in Kelvin and  $R$  is the gas constant. We use  $D_0 = 3.5 \times 10^{-9} \text{ m}^2/\text{s}$  and  $E = 274.19 \text{ kJ/mol}$  for garnet (Ganguly et al., 1998) and  $D_0 = 6.22 \times 10^{-15} \text{ m}^2/\text{s}$  and  $E = 161.5 \text{ kJ/mol}$  for clinopyroxene (Azough and Freer, 2000). As we know the grain sizes of clinopyroxene and garnet in the xenoliths, we can calculate the time it would take Fe to diffuse from crystal cores to rims as a function of temperature from the relationship:

$$x \sim [D(T)t]^{0.5}$$

which can be rearranged to:

$$t \sim x^2/D(T)$$

where  $t$  is time in seconds. Grain radii ( $x$ ) range from 0.5 to 4 mm for clinopyroxene and from 0.5 to 6 mm for garnet in the samples used for these calculations. In Supplemental Figure S10b, we calculate time scales of Fe diffusion as a function of temperature over these length scales. These back-of-the-envelope calculations show that, over time scales relevant for the xenolith suite being incorporated into

the host melt and brought to the surface (days to weeks), Fe should not be lost from clinopyroxene or garnet due to diffusive exchange, as this would take on the order of thousands of years.

**Choice of modeling software and thermodynamic models:** As amphibole is a critically important phase for our dehydration model, we needed to use software with an appropriate thermodynamic amphibole model. The presence of amphibole in samples yielding intermediate to high garnet-clinopyroxene equilibrium pressures (approximately 1.0-1.8 GPa, Figure 5a) necessitated using modeling software that can stabilize amphibole over a wide range of crustal depths. As the MELTS software package is known to have issues stabilizing amphibole, we decided to use Perple\_X modeling. A simple exercise, in which we take the starting compositions used for the equilibrium phase relations experiments of Blatter et al. (2023) and calculate the equilibrium assemblage at the same pressures and temperatures employed in the experiments, demonstrates the advantages of using Perple\_X over MELTS (Fig. S9). Note that MELTS fails to predict amphibole saturation for all experiments equilibrated at pressures over 1 GPa, while Perple\_X more accurately reproduces the observed modal proportion of amphibole observed in the experiments conducted between 1.2 and 1.46 GPa.

The activity-composition relationships for solid solution phases used in our Perple\_X calculations were as follows:

- Amphibole: Green et al. (2016)
- Plagioclase: Holland and Powell (2003)
- Biotite: Holland et al. (2018)
- Clinopyroxene: Holland et al. (2018)
- Orthopyroxene: Holland et al. (2018)
- Olivine: Holland et al. (2018)
- Garnet: Holland et al. (2018)
- Spinel: Holland et al. (2018)
- Epidote: Holland and Powell (1998)
- Phengite: Holland and Powell (1998)
- Ilmenite: White et al. (2014)
- Melt: Holland et al. (2018)

The phases quartz, rutile, sphene, kyanite, sillimanite, andalusite, and water were also considered in our models. Although scapolite is a modally abundant phase in many Mercaderes xenoliths, CO<sub>2</sub> was not included in our Perple\_X modeling. In all models, we run our calculations in the chemical system K<sub>2</sub>O–Na<sub>2</sub>O–CaO–FeO–MgO–Al<sub>2</sub>O<sub>3</sub>–SiO<sub>2</sub>–H<sub>2</sub>O–TiO<sub>2</sub>–Fe<sub>2</sub>O<sub>3</sub> (KNCFMASHTO).

**Fractional crystallization modeling:** The starting composition for the Perple\_X fractional crystallization model represents an average of four primitive Colombian basalt compositions taken from the GEOROC Northern Andean Volcanic Zone basalt/basaltic andesite compilation (Fig. S11). These data are from Marriner and Millward (1984) (sample GV 100C), Kerr et al. (1996) (sample AN173), and Villagomez et al. (2011) (samples DV111 and DV112). These samples have 9-10 wt.% MgO, high Ni (115-250 ppm), and high Cr (200-460 ppm). This basalt was fractionated along the Mercaderes geothermal gradient from 1300 °C and 2 GPa to 800 °C and 1 GPa. We started our model with an initial  $f_{O_2}$  of FMQ+1 and a water content of 3 wt.%. Oxygen fugacity was not fixed during the modeling, and Fe speciation for the system changed as cumulates with varying Fe<sup>+3</sup>/ΣFe ratios were removed. The model

ran down temperature with a 2 °C step size and down pressure with a 40 bar step size. We also ran eight sensitivity tests for this model, varying the initial water content (2-6 wt.%), composition (Mg-andesite to high-Mg basalt), amphibole and clinopyroxene force constant estimates ( $\langle F \rangle_{\text{amph}}$  from 211 to 253 N/m,  $\langle F \rangle_{\text{cpx}}$  from 210 to 244 N/m), and initial oxygen fugacity (FMQ to FMQ+2). The results of these tests are shown in Supplemental Figure S13, both in terms of the bulk Fe isotope composition of the cumulate and the composition of the constitute minerals. All models start with an initial  $\delta^{56}\text{Fe}$  of 0.0‰. While some of these models reproduce specific characteristics of the Mercaderes suite (e.g., relatively unfractionated bulk  $\delta^{56}\text{Fe}$ , observed modal mineralogy), none of them reproduced all the observed characteristics of the Mercaderes suite.

Models run at higher water contents (> 4 wt.% H<sub>2</sub>O) produced less fractionated Fe isotope trends with respect to bulk rock compositions (0.18 - 0.20‰ variability in whole-rock  $\delta^{56}\text{Fe}$ , Fig. S11a). This results from a lowering of the liquidus temperature (from 1330 °C at 2 wt.% H<sub>2</sub>O to 1190 °C at 6 wt.% H<sub>2</sub>O), a decrease in the temperature interval of garnet-dominated fractionation (occurring over a 350 °C temperature range at 2 wt.% H<sub>2</sub>O and a 140 °C temperature range at 6 wt.% H<sub>2</sub>O), and slightly earlier amphibole saturation (920 °C at 2 wt.% H<sub>2</sub>O vs. 950 °C at 6wt% H<sub>2</sub>O) with increased water content. As a result, the amount of garnet relative to amphibole and clinopyroxene fractionated is lower in these more hydrous systems. While higher water contents during crystallization may result in less isotopically fractionated cumulates overall, models with >4 wt.% H<sub>2</sub>O do not produce plagioclase over the investigated pressure-temperature range, in contrast to the observed Mercaderes petrography. These more hydrous models also fail to reproduce the observed trends in garnet Fe isotope chemistry (i.e., increasingly negative  $\delta^{56}\text{Fe}$  with decreasing temperature, Fig. S13b).

Relatively unfractionated bulk rock compositions (0.19‰ variability in whole-rock  $\delta^{56}\text{Fe}$ ) are also produced when we use a more mafic starting composition (sample 014B; Grösser et al., 1989) (Fig. S13c). Compared to the average Colombian basalt composition used in the main text, this starting composition has slightly more MgO (10.2 wt.% vs 9.1 wt.%), resulting in increased clinopyroxene fractionation relative to garnet. As our clinopyroxene force constant (227 N/m) is closer to the force constant of the melt in this model (225 to 240 N/m) than that of garnet (110 N/m), increased clinopyroxene fractionation relative to garnet results in less melt-cumulate fractionation over the investigated pressure-temperature range. Note that within all sensitivity tests and the model presented in the main text,  $\delta^{56}\text{Fe}$  of the instantaneous cumulate composition changes rapidly, whereas  $\delta^{56}\text{Fe}$  of the melt evolves gradually. This is a mass-balance effect and is to be expected because, at high melt fractions, the majority of Fe in the system will remain within the melt. For each 2°C fractionation step in the model, the melt comprises 99-97% of the system's total mass. Therefore, while the composition of the fractionating cumulate may change rapidly as new phases saturate, the composition of the melt should change slowly as these small cumulate masses are removed from the system.

In general, these models suggest that fractional crystallization over a range of  $f\text{O}_2$ s, water contents, and initial starting compositions will result in isotopically fractionated cumulate composition and isotopically heavy late-stage melts (Fig. S14). Prolonged garnet fractionation at high pressures and temperatures depleted later-stage melts in light isotopes of Fe, resulting in the production of isotopically heavy amphibole-bearing cumulates and lower pressures and temperatures.

***Amphibole dehydration model:*** In testing the sensitivity of our amphibole dehydration model, we varied the initial  $\text{Fe}^{3+}/\Sigma\text{Fe}$  ratio from 0.15 to 0.30, the initial water content from 0.5 to 1.5 wt.% H<sub>2</sub>O, the starting composition (diorite XC-MG-5, XC-M-1, or an average of the two samples), amphibole and clinopyroxene force constant estimates ( $\langle F \rangle_{\text{amph}}$  from 211 to 253 N/m,  $\langle F \rangle_{\text{cpx}}$  from 210 to 244 N/m), the threshold at which melt is extracted from the residue (4 to 10 wt.% melt), and the amount of melt

remaining in the residue after each melt extraction event (1 to 0.1 wt.% melt). As in our fractional crystallization model, oxygen fugacity was not fixed during partial melting. The model ran up temperature with a 2 °C step size and up pressure with a 40 bar step size. The results of these sensitivity tests, with respect to the residue composition, are shown in Supplemental Figure S15. While we vary the initial H<sub>2</sub>O content from 0.5 to 1.5 wt.% to assess the effects of water content more robustly on these models, we do not consider the full extent of this range to be strictly appropriate. Given that F and Cl concentrations in amphibole from the diorite are either at or below our detection limits, we assume the primary volatile species in the amphibole structure is water (~2 wt.% H<sub>2</sub>O). As diorite contains 50-60% amphibole and 40-50% plagioclase, and assuming plagioclase contains negligible water, we consider initial water contents of 1.0-1.2 wt.% as the most appropriate estimates for our model and thus opt to use a value of 1.2 in the model presented in the main text.

All models show similar trends, with the solidus varying from 664 to 920 °C and the total amount of melt generated varying from 34 to 41 wt.%. Amphibole and plagioclase are exhausted from all metamorphic residues between 1058-1210 °C and 1084 - 1270 °C, respectively. The final metamorphic product is a residue composed entirely of garnet and clinopyroxene. Partial melting results in limited isotopic depletion of the original metamorphic protolith for all models, with  $\delta^{56}\text{Fe}$  of the residue decreasing by 0.02 to 0.03‰ (Fig. S15). With respect to major elements, partial melting results in a decrease in Na and Ti concentrations and an increase in Fe and Mg. The final metamorphic residues produced at 2 GPa and 1300 °C are similar in major element contents to the Mercaderes garnet clinopyroxenite, albeit with slightly higher Na<sub>2</sub>O. Both major fractional crystallization and amphibole dehydration models also produced metamorphic residues that would be gravitationally unstable with respect to the underlying mantle (Figure 9 of main text).

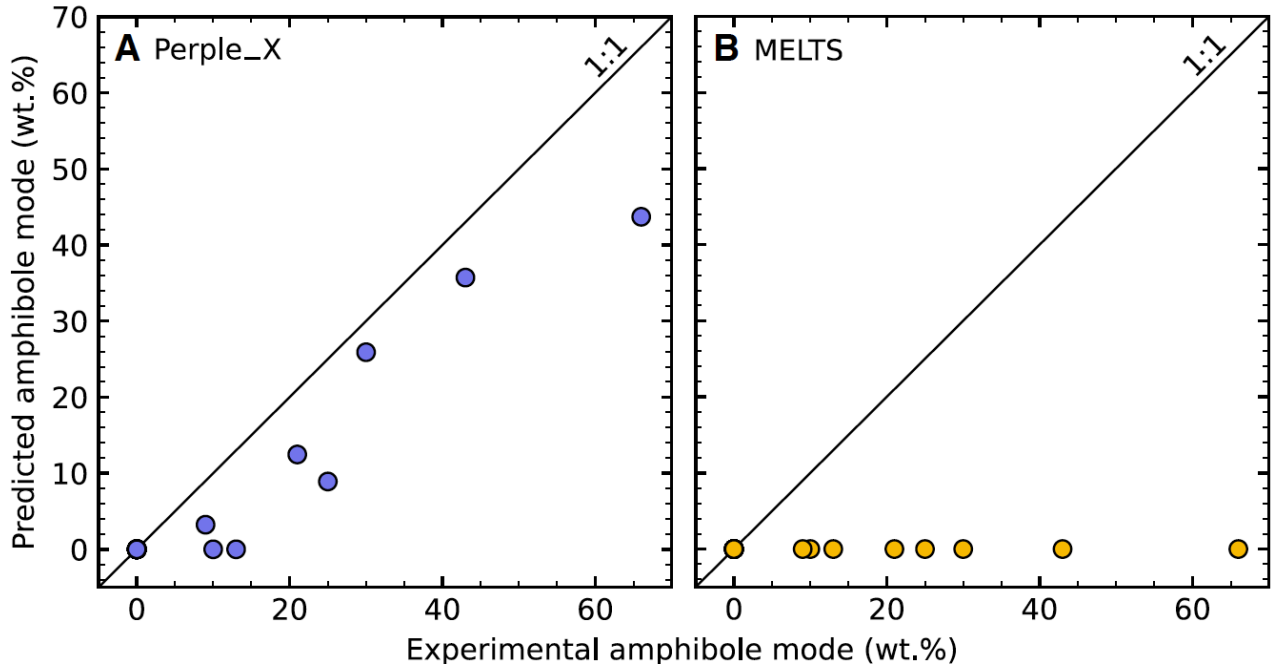


**Figure S9:** Modal abundances of amphibole (wt.%) observed in 1.2 – 1.67 GPa experiments of Blatter et al. (2023) compared to values predicted by Perple\_X (A) and MELTS (B).

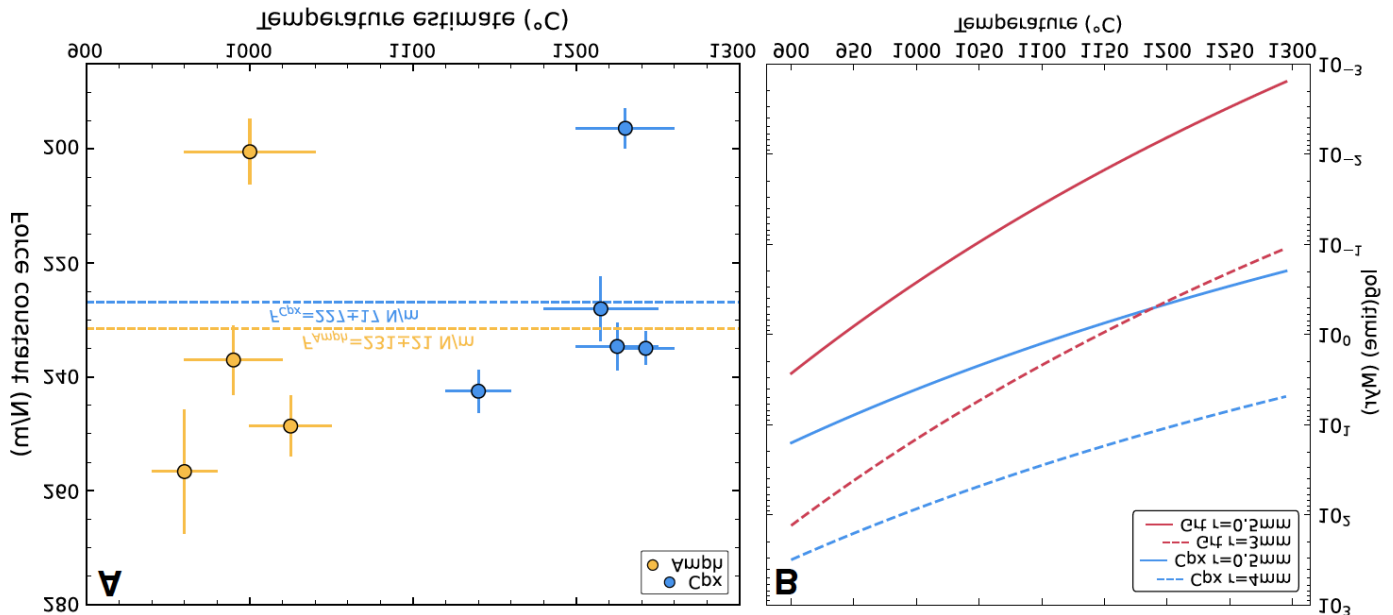


**Figure S10: A)** Force constant estimates for amphibole and clinopyroxene as a function of equilibrium temperature for the Mercaderes xenoliths. **B)** Time scales (shown as log millions of years) for Fe to diffuse from clinopyroxene and garnet crystals with radii ranging from 0.5 to 4 mm and 0.5 to 3 mm, respectively.

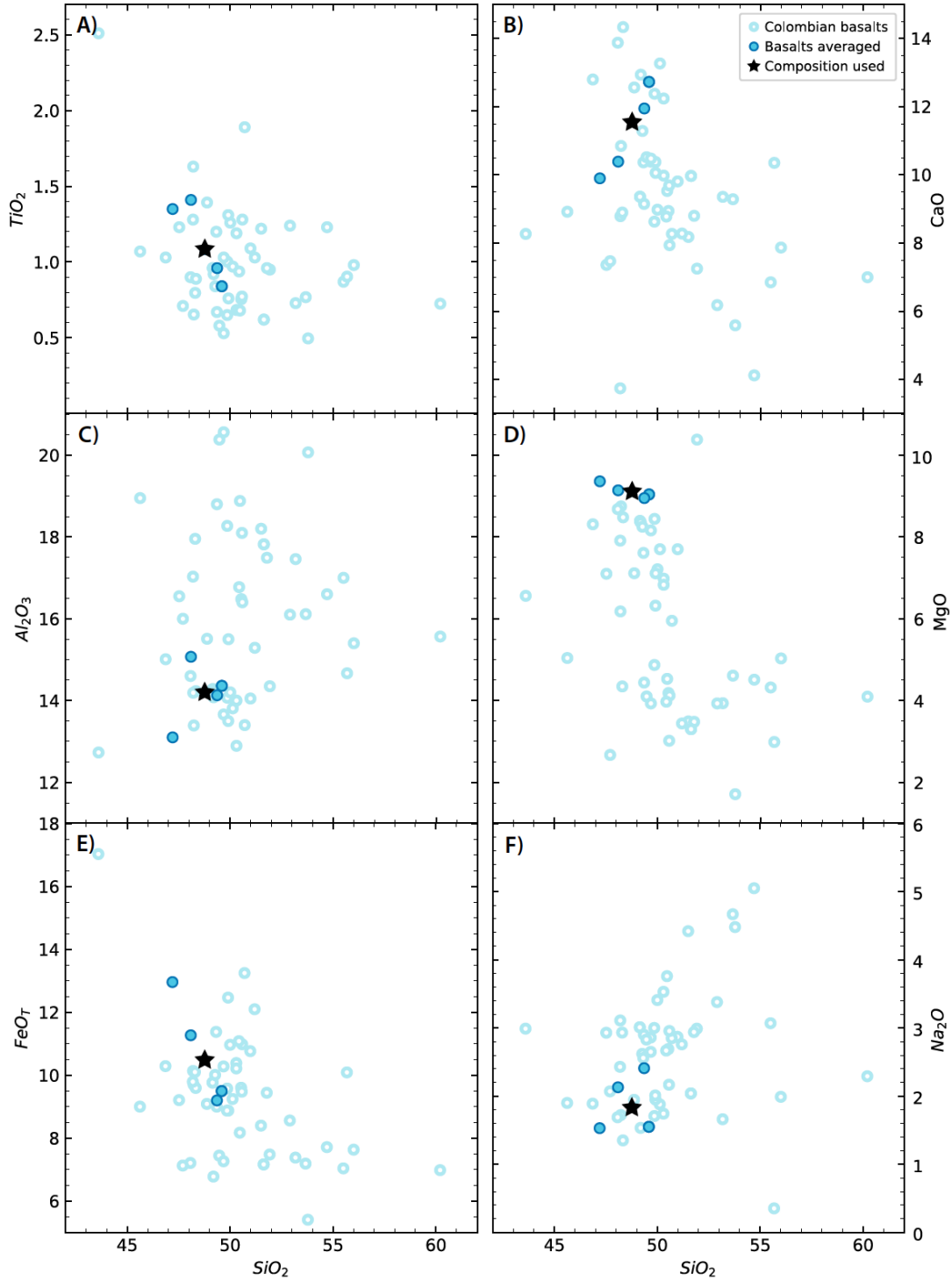


**Figure S11:** Lava used in fractional crystallization modeling. Open circles represent Pre-compiled Northern Andean Volcanic Zone basalt/basaltic andesite compilation from GeoRoc. Filled circles represent high-MgO (9-10 wt.% MgO) basalts averaged to form the starting composition used in our fractional crystallization model (filled star). The basalt compositions we averaged are from Marriner and Millward (1984), Kerr et al. (1996), and Villagomez et al. (2011).

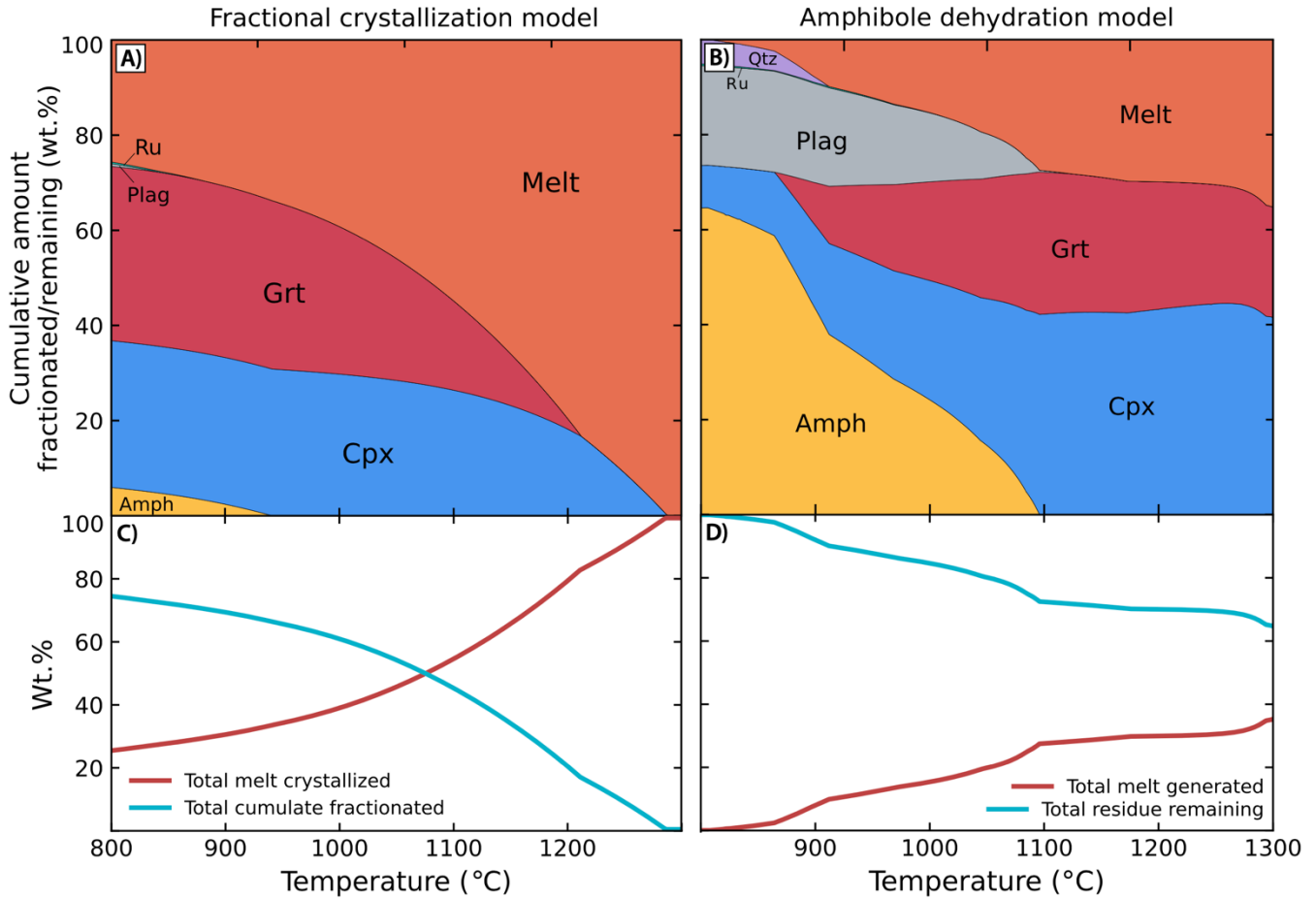


**Figure S12:** Additional modeling results. A) cumulative amount of clinopyroxene, garnet amphibole, rutile, and plagioclase crystallized in fractional crystallization model (as presented in the main text with initial  $fO_2 = FMQ+1$ , initial  $H_2O = 3$  wt.%). B) Total amount of melt generated and amount of clinopyroxene, garnet amphibole, rutile, quartz, and plagioclase present in the residue for amphibole dehydration model (for diorite XC-MG-5 with initial  $Fe^{+3}/\Sigma Fe = 0.30$  and  $H_2O = 1.2$  wt.%). C) Total amount of melt remaining and amount of cumulate crystallized (by mass) as a function of temperature in fractional crystallization model. D) Total amount of melt generated and amount of residue remaining (by mass) as a function of temperature in the amphibole dehydration model.

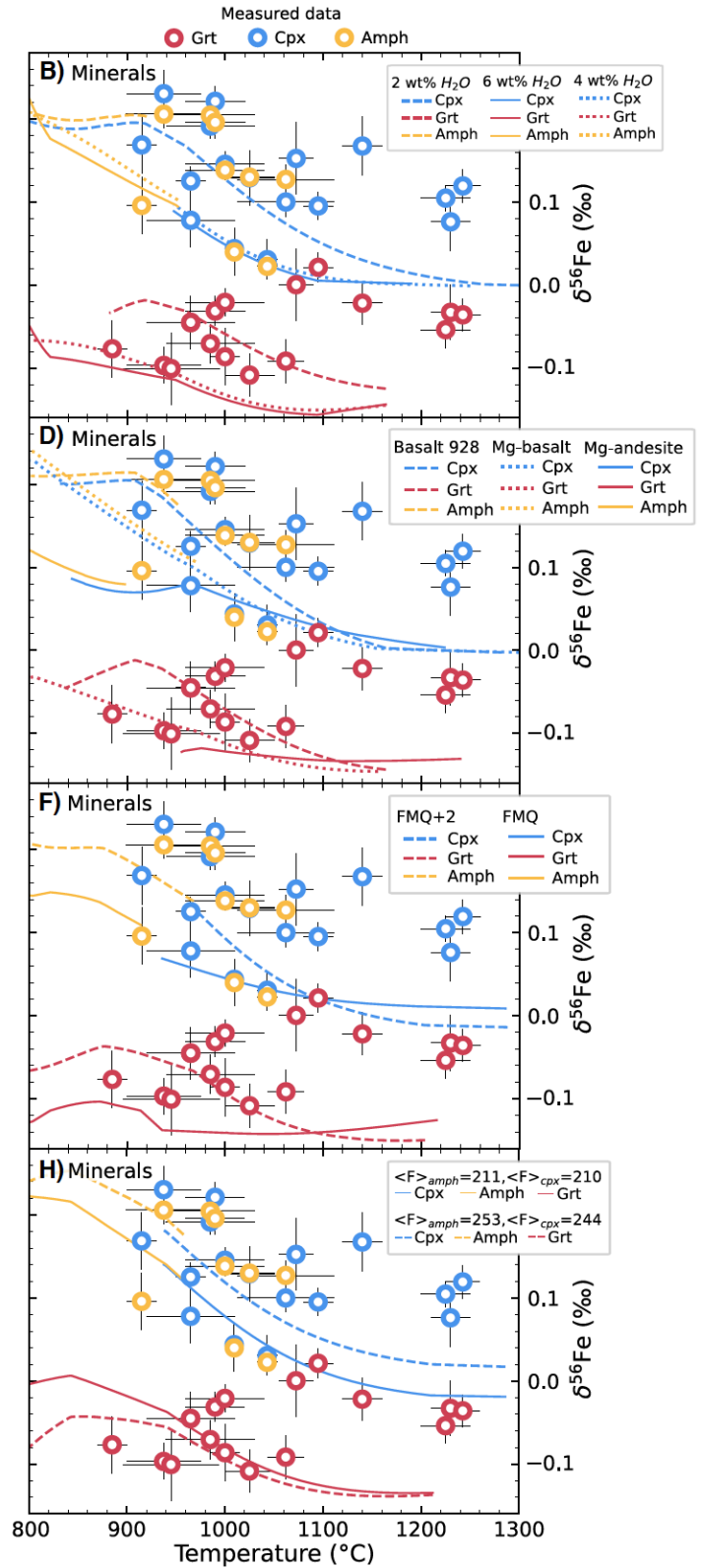
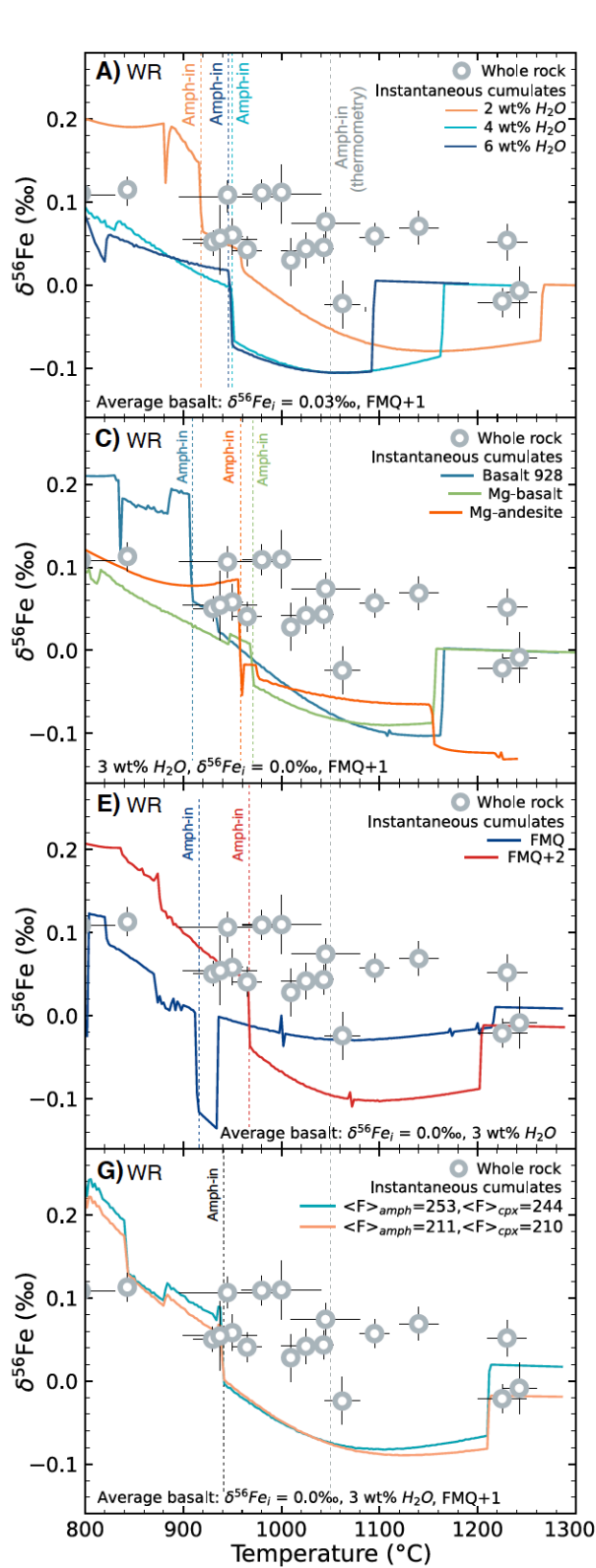


**Figure S13:** (previous page) - sensitivity tests for fractional crystallization models. Oxygen fugacity, melt composition, and water content are varied in these models. Dotted vertical lines denote the temperature and which amphibole enters the crystallizing assemblage for each model and are compared to the minimum temperature at which mineral equilibria thermometry and Perple\_X model for the Mercaderes samples suit suggest amphibole should enter the assemblage (~1050 °C). **(A)** Whole-rock instantaneous Fe isotope composition of cumulates for fractional crystallization of an average Colombian basalt at FMQ+1 for 2, 4, and 6 wt.% initial H<sub>2</sub>O. Complementary mineral Fe isotope compositions for each model are shown in **(B)** and compared to measured mineral values. **(C)** Whole-rock instantaneous Fe isotope cumulate compositions from fractional crystallization models of Mercaderes basalt 928 (Weber, 1998), an average Colombian high-Mg andesite, and a representative Colombian Mg-basalt (sample 014B; Grösser et al., 1989). Complementary mineral Fe isotope compositions for these models are given in **(D)**. The effects of varying oxygen fugacity from FMQ to FMQ+2 on the instantaneous Fe isotope cumulate composition of our average Colombian basalt with 3 wt.% initial H<sub>2</sub>O is shown in **(E)**, with the complementary Fe isotope compositions of minerals in the cumulates shown in **(F)**. The force constants for amphibole and clinopyroxene are varied in **(G)** and **(F)** to reflect the uncertainties in our estimates, with  $\langle F \rangle_{\text{amph}}$  ranging from 211 to 253 N/m and  $\langle F \rangle_{\text{cpx}}$  from 210 to 244 N/m. All other model parameters are the same as in Figure 6 of the main text.

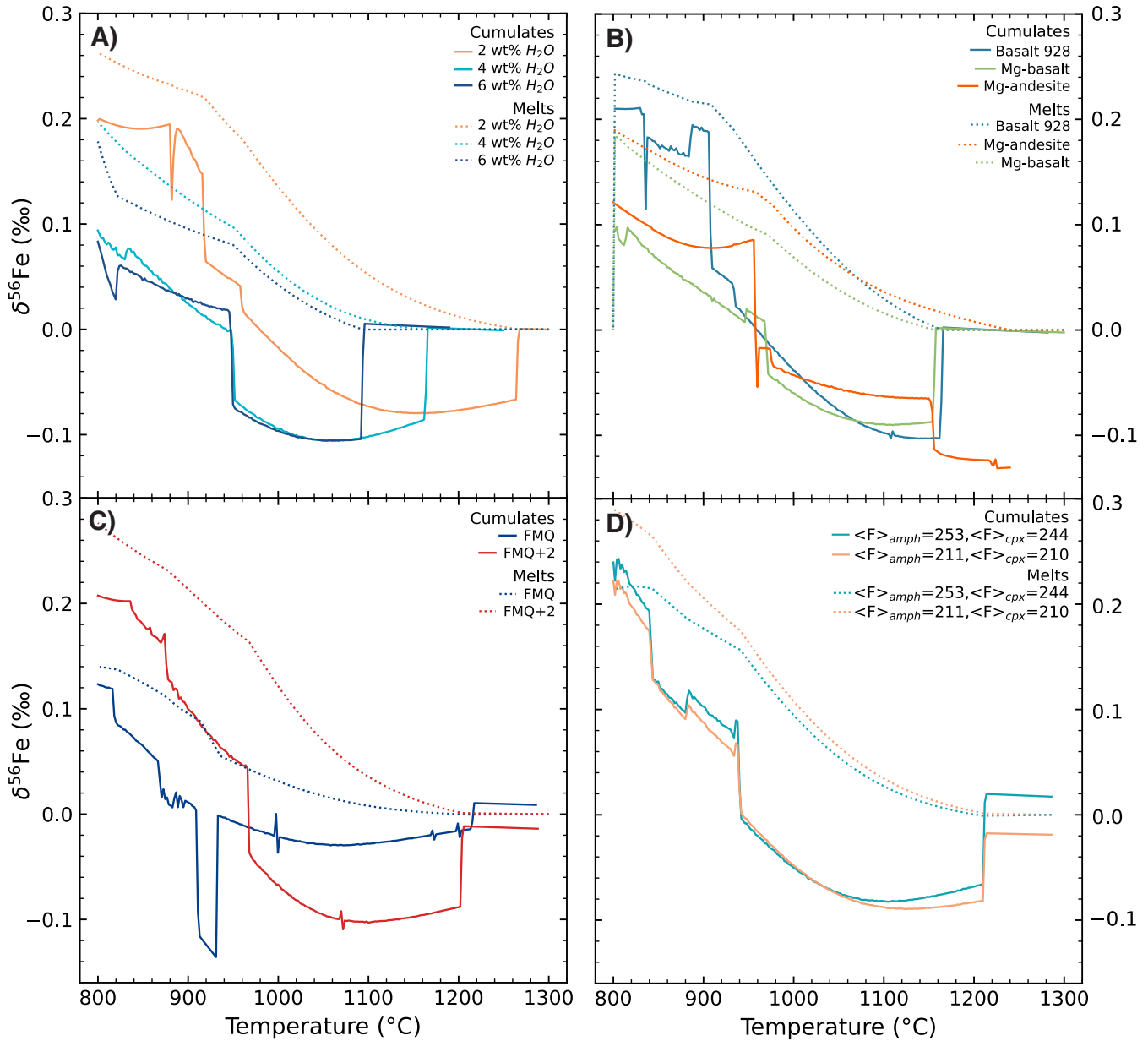


**Figure S14:** Evolution of cumulates (solid lines) and their parental melts (dotted lines) in Perple\_X fractional crystallization modeling in sensitivity tests. **A)** Cumulate and melt Fe isotope composition for fractional crystallization of an average Colombian basalt at FMQ+1 for 2, 4, and 6 wt.% initial H<sub>2</sub>O. **B)** Cumulate and melt  $\delta^{56}\text{Fe}$  for fractional crystallization of Mercaderes basalt 928 (Weber, 1998), an average Colombian high-Mg andesite, and a representative Colombian Mg-basalt (sample 014B; Grösser et al., 1989), all with an initial H<sub>2</sub>O of 3 wt.%. **C)** Cumulate and melt Fe isotope composition for fractional crystallization of an average Colombian basalt with 3 wt.% H<sub>2</sub>O varying  $f\text{O}_2$  from FMQ to FMQ+2. **D)** Fe isotope composition of cumulates and melts varying  $\langle F \rangle_{\text{amph}}$  from 211 to 253 N/m and  $\langle F \rangle_{\text{cpx}}$  from 210 to 244 N/m. All other model parameters are the same as in Figure 6 of the main text (average Colombian basalt from Supplemental Figure S11 used as starting composition, with 3 wt.% H<sub>2</sub>O, and  $f\text{O}_2 = \text{FMQ}+1$ ).

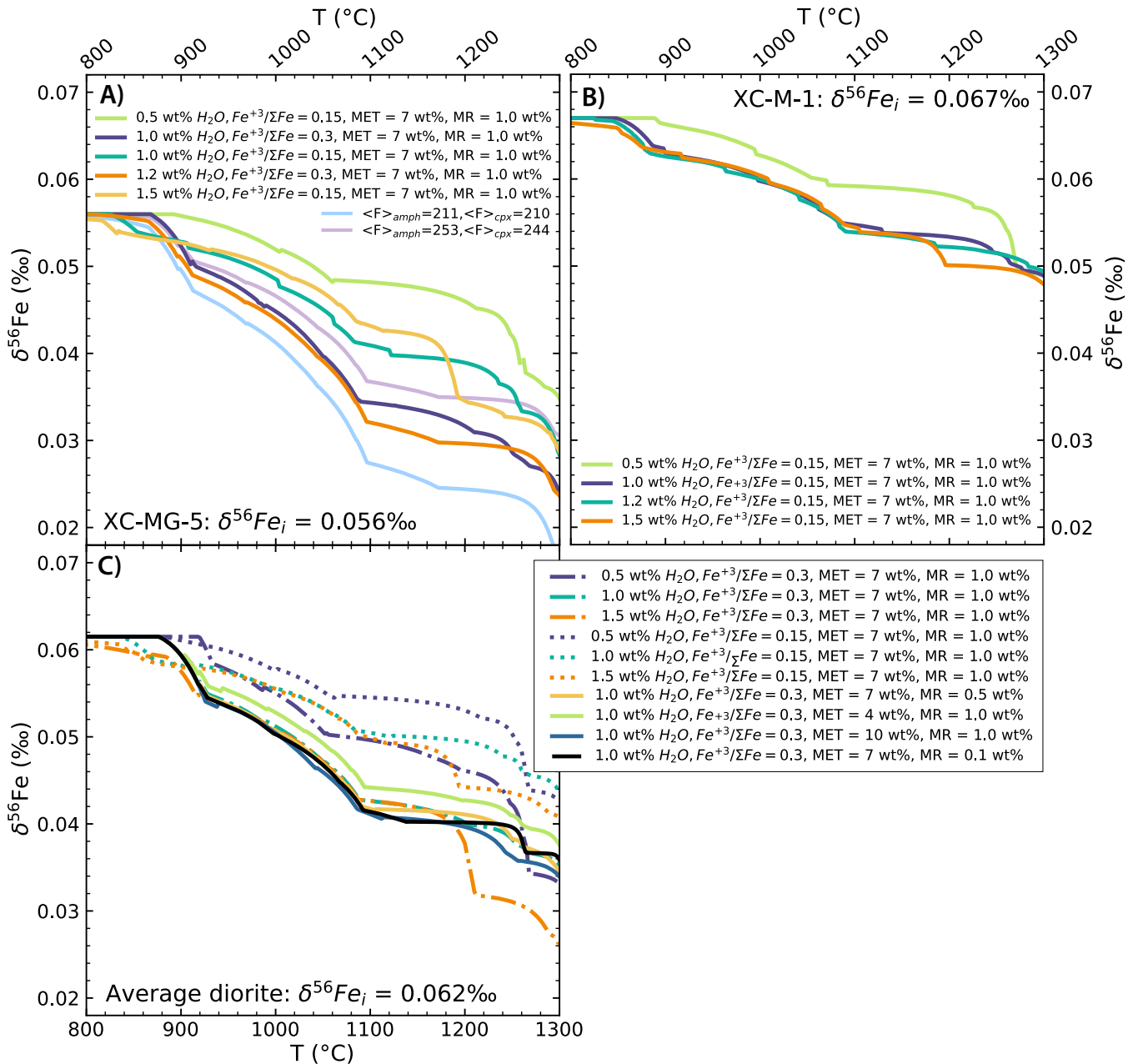


**Figure S15:** Sensitivity tests for amphibole dehydration model showing the range of possible metamorphic residue compositions. Initial composition (XC-M-1, XC-MG-5, or average Mercaderes diorite), initial water content (0.5-1.5 wt.%), initial  $\text{Fe}^{+3}/\Sigma\text{Fe}$  (0.15-0.3), melt mass extraction threshold (MET) (4-10 wt.%), and the mass of melt left in the residue after each extraction event (MR) (0.1 to 1 wt.%) are varied in these models. In (A), for the test where we vary  $\langle F \rangle_{\text{amph}}$  and  $\langle F \rangle_{\text{cpx}}$ , all parameters except force constant are the same as they are in the model we present in Figure 7 of the main text.

Mineral composition isopleths examples

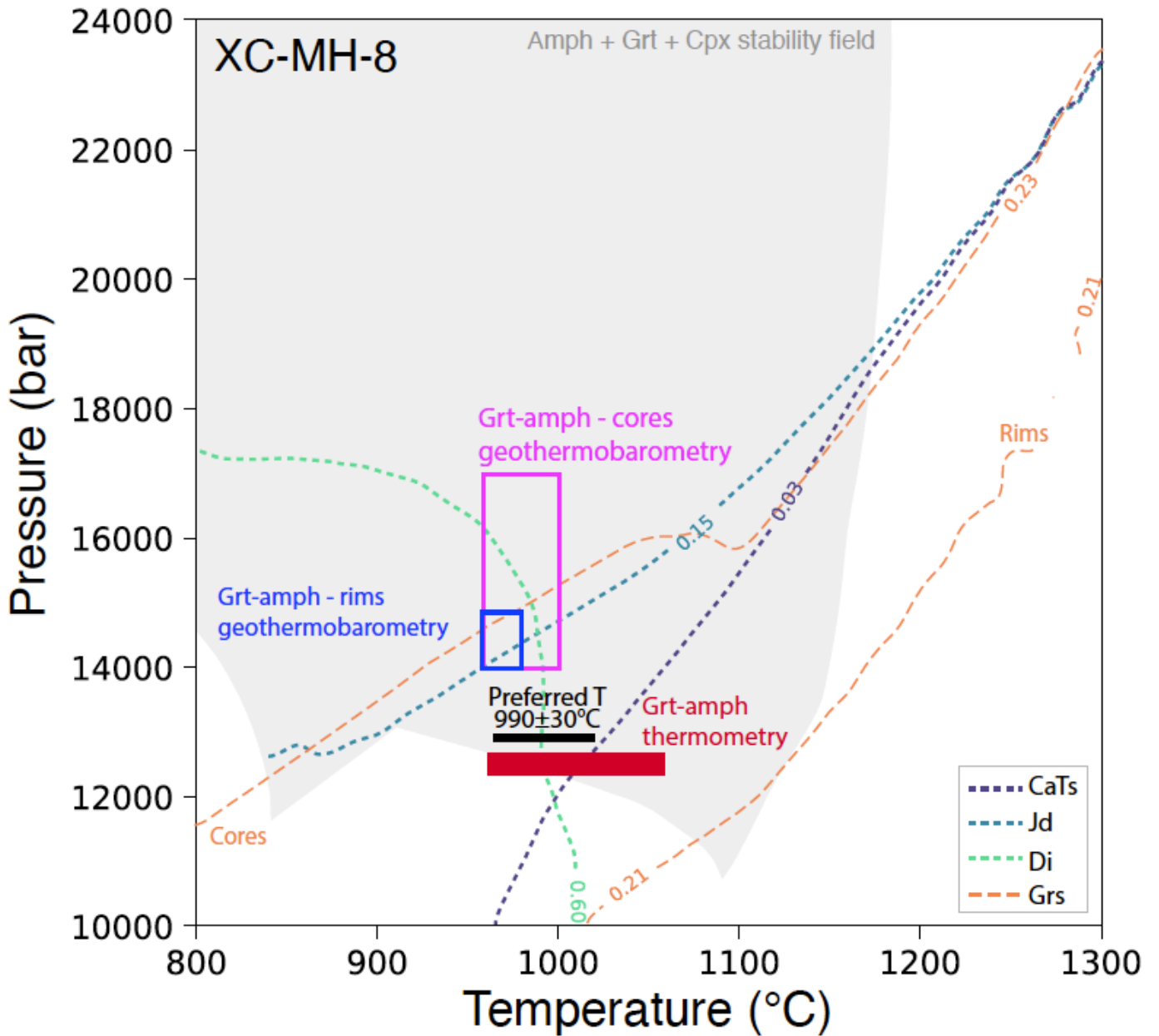


**Figure S16:** Mineral composition isopleths of jadeite (Jd), diopside (Di), calcium tschermakite (CaTs), and grossular (Grs) for sample XC-MH-8 compared to geothermobarometry estimates. The *Perple\_X* amphibole + garnet + clinopyroxene stability field for the XC-MH-8 whole-rock composition is also shown for context.

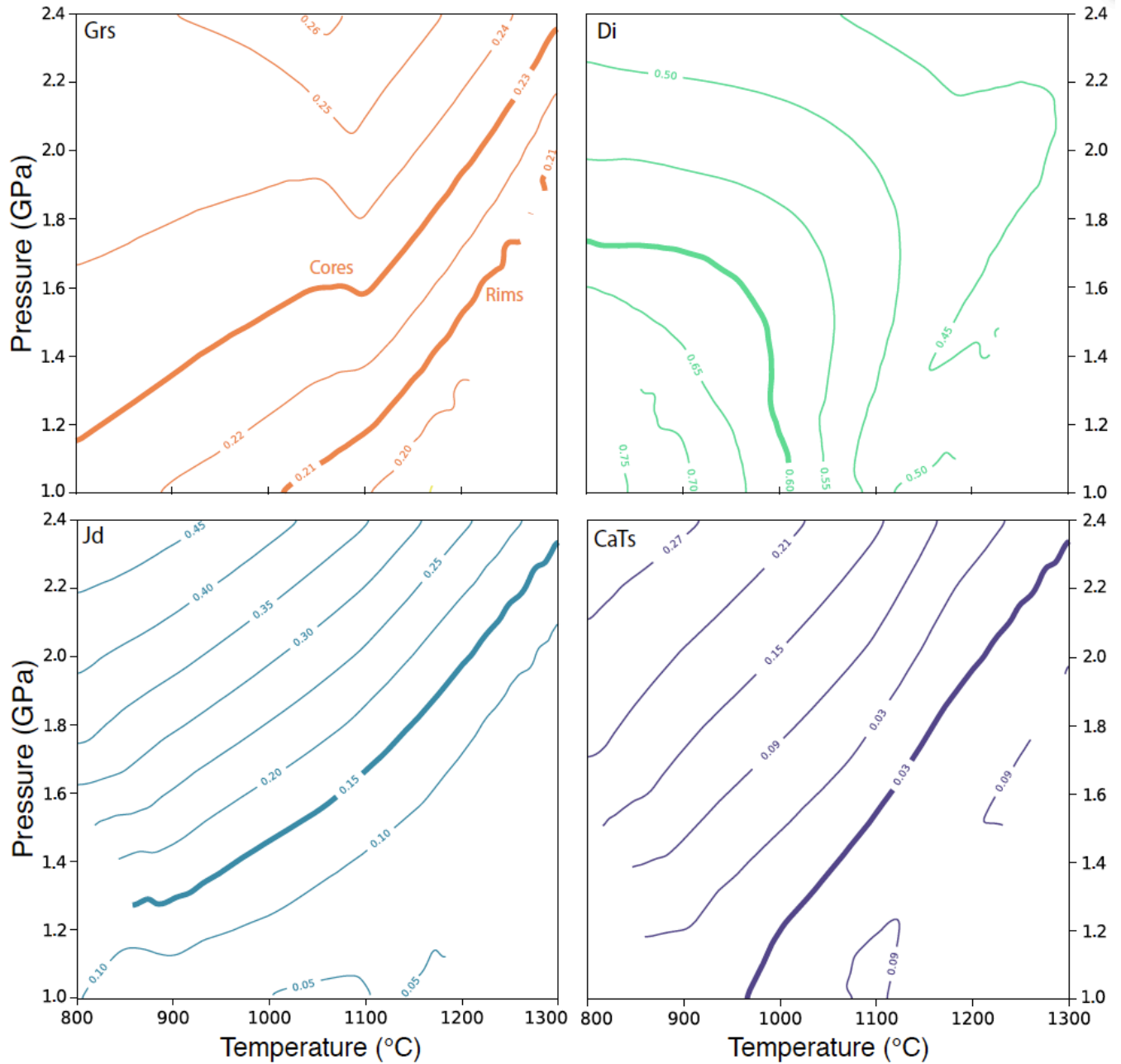


**Figure S17:** Mineral composition isopleths of jadeite (Jd), diopside (Di), calcium tschermakite (CaTs), and grossular (Grs) for sample XC-MH-8. Bolded lines represent values observed in the sample.

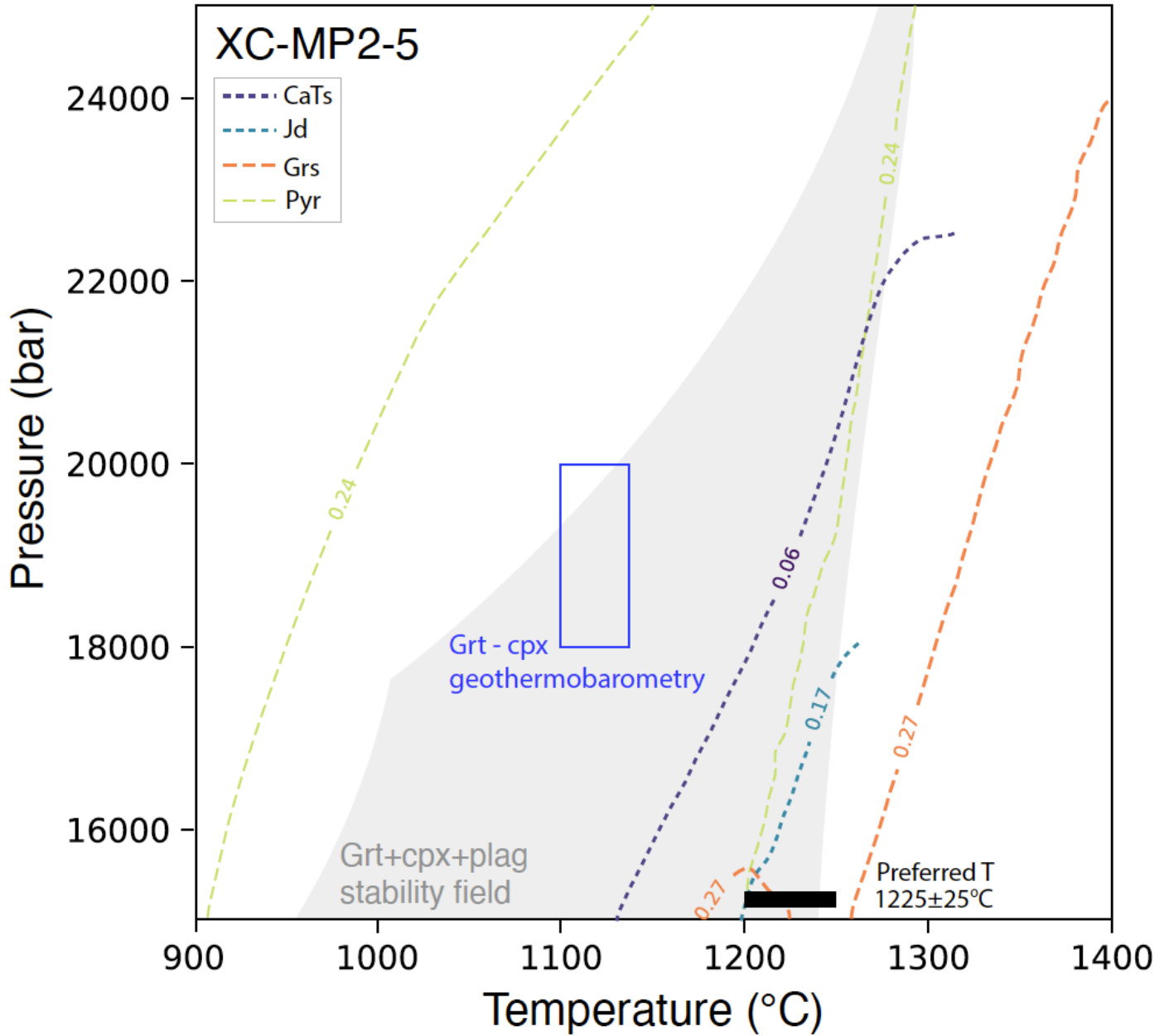


**Figure S18:** Mineral composition isopleths of grossular (Grs), pyrope (Pyr), jadeite (Jd), and calcium tschermakite (CaTs) for sample XC-MP2-5 compared to geothermobarometry estimates. The Perple\_X plagioclase + garnet + clinopyroxene stability field for the XC-MP2-5 whole-rock composition is also shown for context.

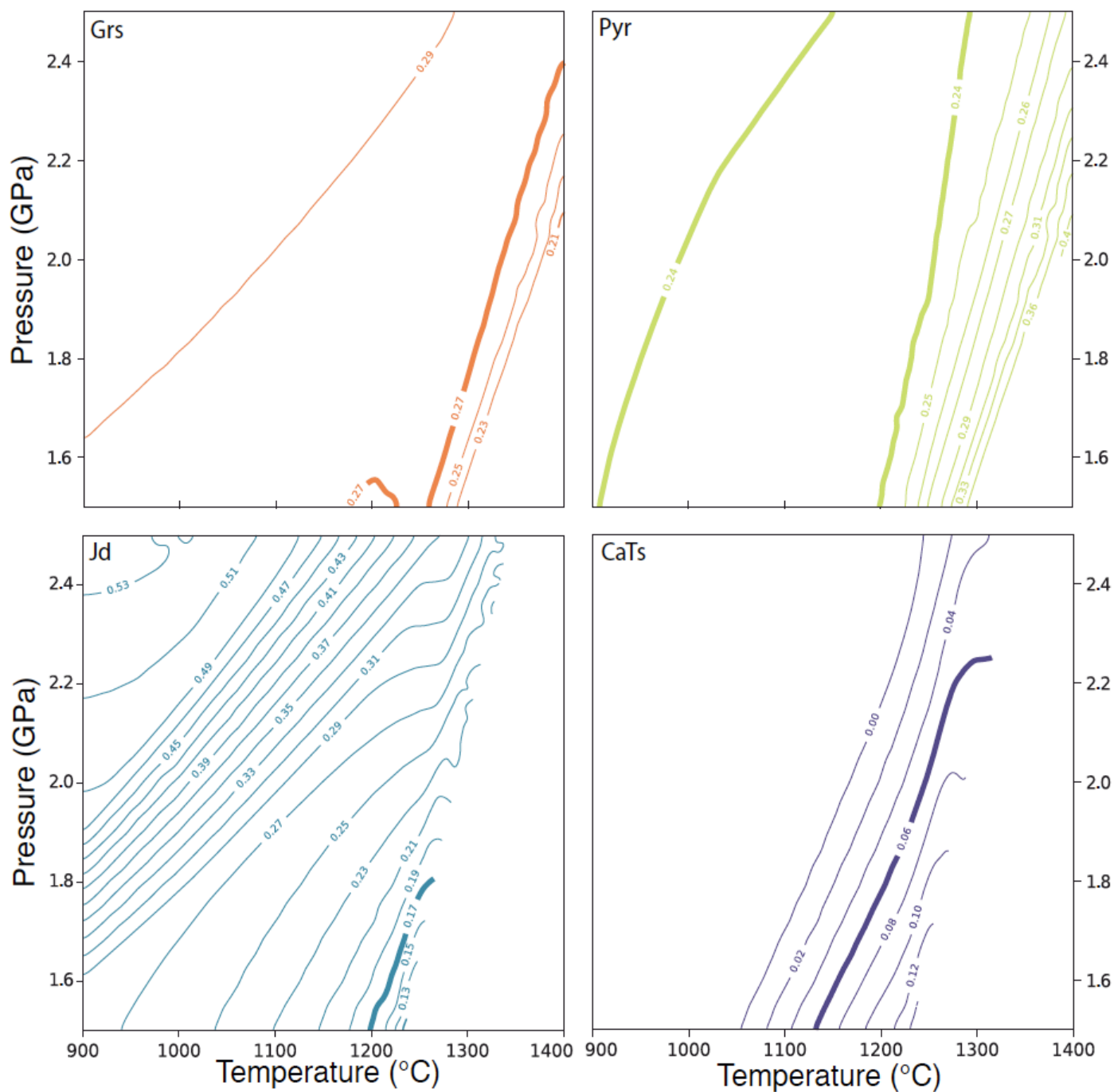


**Figure S19:** Mineral composition isopleths of grossular (Grs), pyrope (Pyr), jadeite (Jd), and calcium tschermakite (CaTs) for sample XC-MP2-5. Bolded lines represent values observed in the sample.

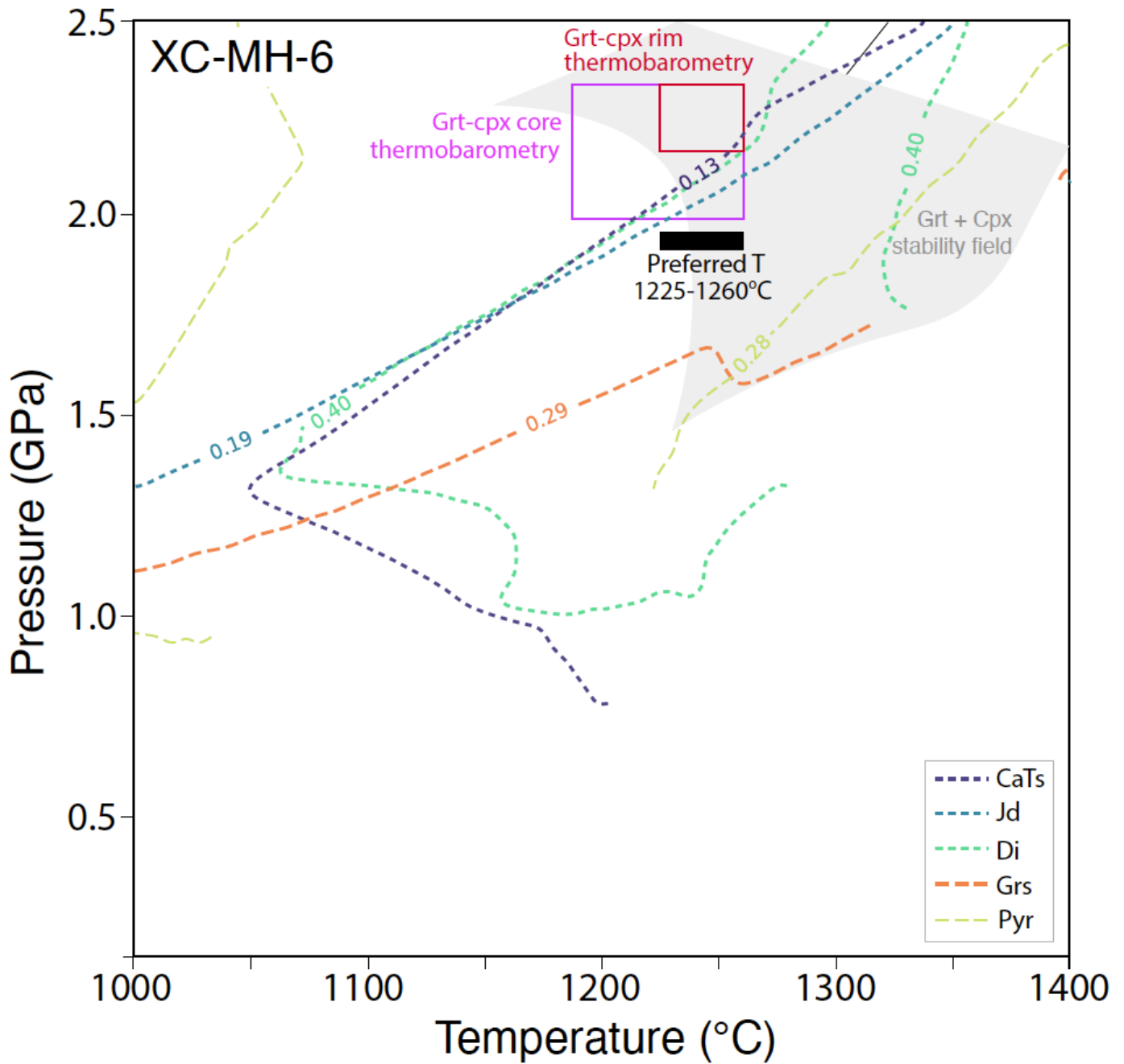


**Figure S20:** Mineral composition isopleths of grossular (Grs), pyrope (Pyr), diopside (Di), jadeite (Jd), and calcium tschermakite (CaTs) for sample XC-MH-6 compared to geothermobarometry estimates. The Peple\_X garnet + clinopyroxene stability field for the XC-MH-6 whole-rock composition is also shown for context.

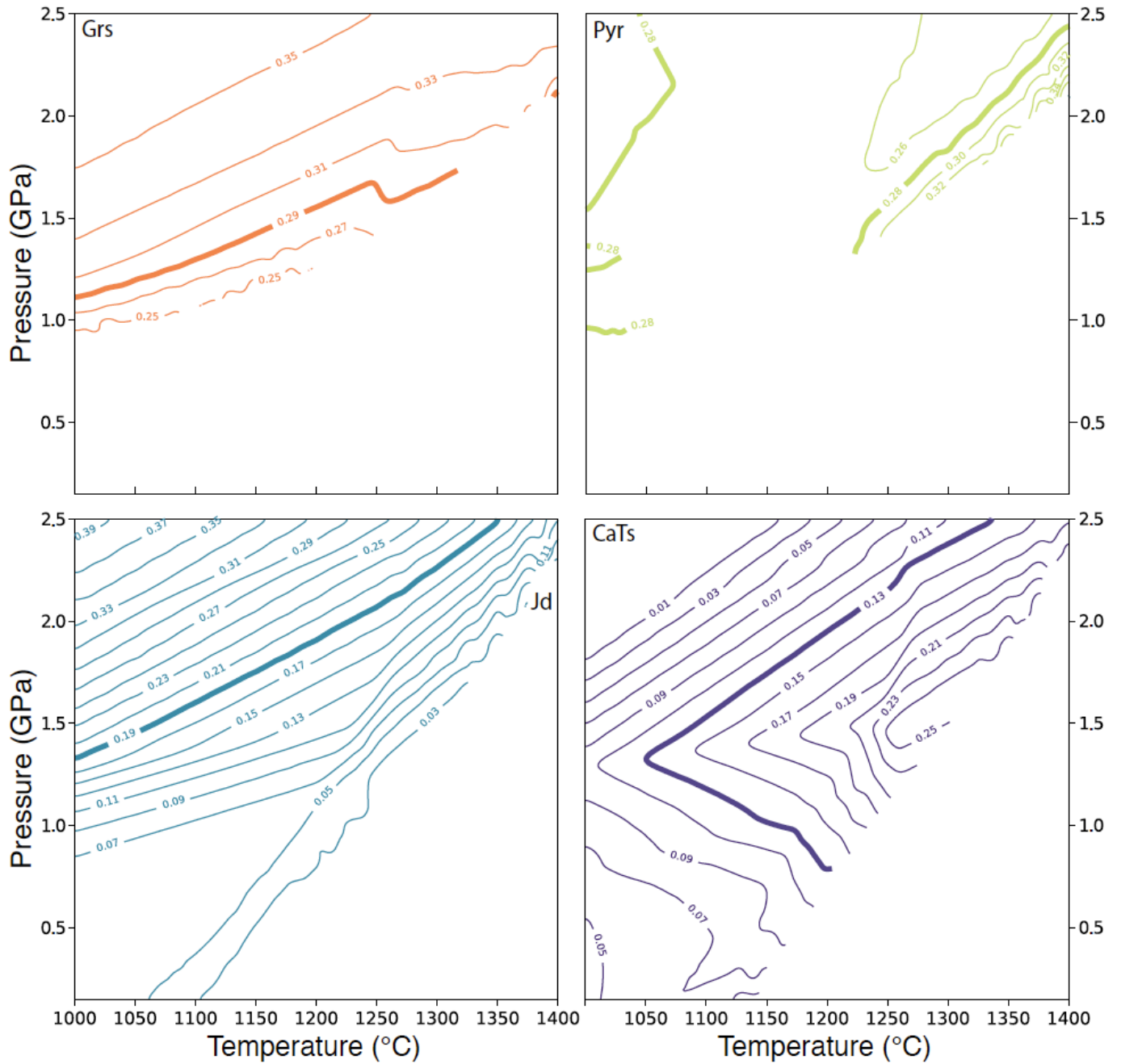


**Figure S21:** Mineral composition isopleths of grossular (Grs), pyrope (Pyr), jadeite (Jd), and calcium tschermakite (CaTs) for sample XC-MH-6. Bolded lines represent values observed in the sample.

**Additional references**

- Abers, G. A., & Hacker, B. R. (2016). A MATLAB toolbox and Excel workbook for calculating the densities, seismic wave speeds, and major element composition of minerals and rocks at pressure and temperature. *Geochemistry, Geophysics, Geosystems*, *17*(2), 616-624.
- An, Y., Huang, J. X., Griffin, W. L., Liu, C., & Huang, F. (2017). Isotopic composition of Mg and Fe in garnet peridotites from the Kaapvaal and Siberian cratons. *Geochimica et Cosmochimica Acta* **200**, 167-185.
- Aoya, M. (2001). P–T–D path of eclogite from the Sambagawa belt deduced from combination of petrological and microstructural analyses. *Journal of Petrology* **42**(7), 1225-1248.
- Armstrong, J. T. (1995). Citzaf-a package of correction programs for the quantitative Electron Microbeam X-Ray-Analysis of thick polished materials, thin-films, and particles. *Microbeam Analysis* **4**(3), 177-200.
- Azough, F., & Freer, R. (2000). Iron diffusion in single-crystal diopside. *Physics and Chemistry of Minerals* **27**, 732-740.
- Beard, B. L., & Johnson, C. M. (2004). Inter-mineral Fe isotope variations in mantle-derived rocks and implications for the Fe geochemical cycle. *Geochimica et Cosmochimica Acta* **68**(22), 4727-4743.
- Dauphas, N., John, S. G., & Rouxel, O. (2017). Iron isotope systematics. *Reviews in Mineralogy and Geochemistry* **82**(1), 415-510.
- DeBari, S. M., & Coleman, R. G. (1989). Examination of the deep levels of an island arc: Evidence from the Tonsina ultramafic-mafic assemblage, Tonsina, Alaska. *Journal of Geophysical Research: Solid Earth* **94**(B4), 4373-4391.
- Ganguly, J., Cheng, W., & Chakraborty, S. (1998). Cation diffusion in aluminosilicate garnets: experimental determination in pyrope-almandine diffusion couples. *Contributions to Mineralogy and Petrology* **131**, 171-180.
- Green, E. C. R., White, R. W., Diener, J. F. A., Powell, R., Holland, T. J. B., & Palin, R. M. (2016). Activity–composition relations for the calculation of partial melting equilibria in metabasic rocks. *Journal of Metamorphic Geology*, *34*(9), 845-869.
- Grösser, J. R. (1989). Geotectonic evolution of the Western Cordillera of Colombia: New aspects from geochemical data on volcanic rocks. *Journal of South American Earth Sciences*, *2*(4), 359-369.
- Holland, T. J., Green, E. C., & Powell, R. (2018). Melting of peridotites through to granites: a simple thermodynamic model in the system KNCFMASHTOCr. *Journal of Petrology*, *59*(5), 881-900.
- Holland, T., & Powell, R. (2003). Activity–composition relations for phases in petrological calculations: an asymmetric multicomponent formulation. *Contributions to Mineralogy and Petrology*, *145*, 492-501.

- Holland, T. J. B., & Powell, R. T. J. B. (1998). An internally consistent thermodynamic data set for phases of petrological interest. *Journal of metamorphic Geology*, 16(3), 309-343.
- Jagoutz, O., Müntener, O., Ulmer, P., Pettke, T., Burg, J. P., Dawood, H., & Hussain, S. (2007). Petrology and mineral chemistry of lower crustal intrusions: The Chilas Complex, Kohistan (NW Pakistan). *Journal of Petrology* 48(10), 1895-1953.
- Kerr, A. C., Tarney, J., Marriner, G. F., Nivia, A., Klaver, G. T., & Saunders, A. D. (1996). The geochemistry and tectonic setting of late Cretaceous Caribbean and Colombian volcanism. *Journal of South American Earth Sciences* 9(1-2), 111-120.
- Klein, E. M. (2003). Geochemistry of the igneous oceanic crust. *Treatise on Geochemistry* 3, 659.
- Li, D. Y., Xiao, Y. L., Li, W. Y., Zhu, X., Williams, H. M., & Li, Y. L. (2016). Iron isotopic systematics of UHP eclogites respond to oxidizing fluid during exhumation. *Journal of Metamorphic Geology* 34(9), 987-997.
- Liang, W., Huang, J., Zhang, G., & Huang, F. (2022). Iron isotopic fractionation during eclogite anatexis and adakitic melt evolution: Insights into garnet effect on Fe isotopic variations in high-silica igneous rocks. *Contributions to Mineralogy and Petrology* 177(3), 33.
- Marriner, G. F., & Millward, D. (1984). The petrology and geochemistry of Cretaceous to Recent volcanism in Colombia: The magmatic history of an accretionary plate margin. *Journal of the Geological Society* 141(3), 473-486.
- Morimoto, N. (1989). Nomenclature of pyroxenes. *Mineralogical Journal* 14(5), 198-221.
- Pernet-Fisher, J. F., Howarth, G. H., Liu, Y., Barry, P. H., Carmody, L., Valley, J. W., Taylor, L. A. (2014). Komsomolskaya diamondiferous eclogites: Evidence for oceanic crustal protoliths. *Contributions to Mineralogy and Petrology* 167, 1-17.
- Quinn, R. J., Valley, J. W., Zeb Page, F., & Fournelle, J. H. (2016). Accurate determination of ferric iron in garnets. *American Mineralogist*, 101(7), 1704-1707.
- Schmickler, B., Jacob, D. E., & Foley, S. F. (2004). Eclogite xenoliths from the Kuruman kimberlites, South Africa: Geochemical fingerprinting of deep subduction and cumulate processes. *Lithos* 75(1-2), 173-207.
- Schoenberg, R., Marks, M. A., Schuessler, J. A., von Blanckenburg, F., & Markl, G. (2009). Fe isotope systematics of coexisting amphibole and pyroxene in the alkaline igneous rock suite of the Ilímaussaq Complex, South Greenland. *Chemical Geology* 258(1-2), 65-77.
- Sosa, E. S., Bucholz, C. E., Barickman, M. H., VanTongeren, J. A., Setera, J. B., Kay, S. M., & Kay, R. W. (2023). Petrology and geochemistry of Adak Island plutonic xenoliths: Implications for primitive magma generation and crustal differentiation in the Aleutian Island arc. *Journal of Petrology* 64(10).

Tappe, S., Smart, K. A., Pearson, D. G., Steenfelt, A., & Simonetti, A. (2011). Craton formation in Late Archean subduction zones revealed by first Greenland eclogites. *Geology* **39**(12), 1103-1106.

Tsujimori, T. (2002). Prograde and retrograde PT paths of the late Paleozoic glaucophane eclogite from the Renge metamorphic belt, Hida Mountains, southwestern Japan. *International Geology Review* **44**(9), 797-818.

Viljoen, K. S., Schulze, D. J., & Quadling, A. G. (2005). Contrasting group I and group II eclogite xenolith petrogenesis: Petrological, trace element and isotopic evidence from eclogite, garnet-websterite and alkremite xenoliths in the Kaalvallei kimberlite, South Africa. *Journal of Petrology* **46**(10), 2059-2090.

Viljoen, F., Dobbe, R., Harris, J., & Smit, B. (2010). Trace element chemistry of mineral inclusions in eclogitic diamonds from the Premier (Cullinan) and Finsch kimberlites, South Africa: Implications for the evolution of their mantle source. *Lithos* **118**(1-2), 156-168.

Villagómez, D., Spikings, R., Magna, T., Kammer, A., Winkler, W., & Beltrán, A. (2011). Geochronology, geochemistry and tectonic evolution of the Western and Central cordilleras of Colombia. *Lithos* **125**(3-4), 875-896.

White, R. W., Powell, R. O. G. E. R., Holland, T. J. B., Johnson, T. E., & Green, E. C. R. (2014). New mineral activity–composition relations for thermodynamic calculations in metapelitic systems. *Journal of Metamorphic Geology*, **32**(3), 261-286.

Williams, H. M., Peslier, A. H., McCammon, C., Halliday, A. N., Levasseur, S., Teutsch, N., & Burg, J. P. (2005). Systematic iron isotope variations in mantle rocks and minerals: The effects of partial melting and oxygen fugacity. *Earth and Planetary Science Letters* **235**(1-2), 435-452.

Ye, H., Wu, C., Brzozowski, M. J., Yang, T., Zha, X., Zhao, S., ... & Li, W. (2020). Calibrating equilibrium Fe isotope fractionation factors between magnetite, garnet, amphibole, and biotite. *Geochimica et Cosmochimica Acta* **271**, 78-95.

Zhao, X. M., Zhang, H. F., Zhu, X. K., Zhu, B., & Cao, H. H. (2015). Effects of melt percolation on iron isotopic variation in peridotites from Yangyuan, North China Craton. *Chemical Geology* **401**, 96-110.